ASCE Journal of Geotechnical & Geoenvironmental Engineering, Vol. 143, No. 9,
Download from SCE DOI: http://ascelibrary.org/doi/10.1061/%28ASCE%29GT.1943-5606.0001737

3D Experimental Measurement of Lattice Strain and Fracture Behaviour of Sand Particles Using Synchrotron X-ray Diffraction and Tomography

Mehmet B. Cil[1], Khalid A. Alshibli[2], and Peter Kenesei[3]

ABSTRACT: 3D synchrotron X-ray diffraction (3DXRD) and synchrotron micro-computed tomography (SMT) techniques were used to measure and monitor the lattice strain evolution and fracture behavior of natural Ottawa sand particles subjected to 1D compression loading. The average particle-averaged lattice strain within each sand particle was measured using 3DXRD and then was used to calculate the corresponding lattice stress tensor. In addition, the evolution and mode of fracture of sand particles was investigated using high-resolution 3D SMT images. The results of diffraction data analyses revealed that the major principal component of the lattice strain or stress tensor increased in most of the particles as the global applied compressive load increased until the onset of fracture. Particle fracture and subsequent rearrangements caused significant variation and fluctuations in measured lattice strain/stress values from one particle to another and from one load stage to the next load stage one. SMT image analysis at the particle-scale showed that cracks in fractured sand particles generally initiated and propagated along the plane that connects the two contact points. Fractured particles initially split into two or three major fragments, and in some cases, was followed by disintegration into multiple smaller fragments. Micro-scale analysis of fractured particles showed that particle position, morphology, and the number and location of contact points played a major role in the occurrence of particle fracture in confined comminution of the sand assembly.

Key words: crystal structure, non-destructive, sand fracture, micro-mechanics, tomography

[1] Postdoctoral Research Fellow, Dept. of Civil & Env. Engineering, Technological Institute, 2145 Sheridan Road, Tech A236, Northwestern University, Evanston, IL 60208, USA, Email: mehmet.cil@northwestern.edu
[2] Professor, Department of Civil and Environmental Engineering, University of Tennessee, Knoxville, TN 37996, USA, Email: Alshibli@utk.edu
[3] Research Scientist, Argonne National Laboratory, Argonne, IL 60439, USA, Email: kenesei@aps.anl.gov

Introduction

Granular materials are commonly encountered and used in many engineering applications such as construction, pharmaceutical manufacturing, and mineral processing. The performance of the systems that involve handling and processing of granular materials are generally below design efficiency, which mainly stems from the lack of a comprehensive understanding of the fundamental behavior of granular materials. Granular materials are composed of discrete particles with wide ranges of particle mineralogy, size, impurities, defects, and morphology. Their macroscopic behavior is governed by complex micro-scale interactions of particles including interlocking, rotation, translation and fracture. The majority of current continuum-based constitutive models (e.g., Manzari and Dafalias 1997; Andrade and Borja 2006) are successful in predicting the overall material response; however, they do not take into account the role of particle-scale processes. It is well known that the failure in granular systems that manifests as a shear band or diffuse bifurcation initiates at the micro and meso-scales due to local instabilities. Developing a micromechanics-based constitutive model using particle-scale measurements is essential to fully characterize the deformation behavior of particulate systems.

Particle kinematics, contact characteristics and force transmission mechanisms need to be characterized and quantified to uncover the influence of microscopic mechanisms on granular material response and to develop micromechanics-based constitutive models. However, acquiring such measurements within a particulate system is a challenging task when one uses conventional experimental techniques. New techniques capable of examining the material response at the scale of individual particles has emerged in the last two decades. Significant progress has been made to characterize particle kinematic behavior using advanced 3D imaging techniques such as x-ray computed tomography (CT) and its improved version synchrotron micro-computed tomography

(SMT). These techniques yield 3D images of geomaterials with a resolution high enough for quantitative analysis. SMT and CT have proven to be excellent techniques to monitor deformation mechanisms in geomaterials under various loading conditions (e.g., Lenoir et al. 2007; Hall et al. 2010; Fonseca et al. 2012; Hasan and Alshibli 2012, , Viggiani et al. 2014; Cil et al. 2014) and capture the 3D kinematics (translation and rotation) of individual particles in granular soils with a high accuracy (e.g., Hallet al. 2010; Andò et al. 2012; Druckrey and Alshibli 2014). Although they are powerful, the major shortcoming of these imaging techniques is their inability to measure inter-particle forces and strain within particles. Neutron imaging and diffraction was employed to determine the lattice strain of silica sand and steel balls (Penumadu et al. 2009; Wensrich et al. 2014). This approach required averaging the lattice strain for an assembly of particles within a gauge volume or measuring elastic strain of each particle by employing a gauge volume corresponding to particle size. The evolution of lattice strain/stress for individual particles was not evaluated in these studies.

Recently, 3D synchrotron x-ray diffraction (3DXRD) has emerged as a novel non-destructive technique that measures the volume-averaged lattice strain of individual particles (i.e., the average strain in the crystal lattices of sand particles) within granular specimens composed of few particles (Hall et al. 2011; Alshibli et al. 2013; Cil et al. 2014; Hall and Wright 2015). Lattice strain tensors can be measured experimentally and used to compute the corresponding stress tensor assuming an elastic stress-strain relationship. The computed average lattice stresses within particles will eventually be related to inter-particle contact forces and force chains using 3D finite element analysis. This will provide key information to characterize the force transmission mechanism in granular media. These lattice stress-strain measurements along with the 3D kinematics of particles can provide essential experimental measurements to develop and calibrate

advanced micro-mechanics based constitutive models using real experimental particle-scale measurements. Alshibli, et al. (2013) measured the strain tensor of individual particles in a column composed of three natural silica sand particles subjected to 1D compression. Hall and Wright (2014, 2015) measured the average lattice elastic strain values of 31 synthetic single crystal silica particles in a granular assembly of 96 particles. This paper builds on the work of Alshibli, et al. (2013), and focuses on measuring the particle-averaged lattice strain of a larger number of natural silica sand particles in a specimen that was loaded under 1D compression. In addition, the beamline incorporated SMT capabilities that can image the same specimen. The evolution of particle fracture and deformation characteristics of the sand assembly were investigated using high-resolution 3D SMT images. The volume and kinematic behavior of sand particles acquired from SMT images helped in tracking particles while calculating the volume-averaged strain tensors at different load stages in 3DXRD data analysis. The combination of 3DXRD and SMT techniques provides a unique opportunity to track individual particles and measure their lattice strain data simultaneously. Although the scope of this paper is limited to demonstrating the feasibility of these techniques on a small-size specimen, the measurements reported in this paper are an essential first step for experimental measurements to uncover the complex constitutive behavior of granular materials in future studies. They can also be used to derive and calibrate more physically based constitutive models that incorporate particle-to-particle interaction.

Experiment Description

The experiment was conducted on particles with grain sizes between US Sieve #40 (0.420 mm) and Sieve #50 (0.297 mm) that were sieved from F-75 Ottawa sand; a natural silica sand that was mined and marketed by the US Silica Company. The main constituent of the sand is α-quartz mineral (99%). The 1D compression experiment was conducted using a specially designed test

cell that includes a specimen mold, computer-controlled actuator to apply axial load, two load cells, and a data acquisition system (Figure 1). The specimen mold consisted of an acrylic cylinder with an outer diameter of 15 mm and a 1 mm diameter cylindrical hole at the center to house sand particles. To quantify the friction force between sand particles and the mold, two load cells with a capacity of 355 N (resolution 0.35 N) and 1112 N (resolution 0.56 N) were attached at the top and bottom of the specimen, respectively. The sand particles were rinsed with distilled water and oven-dried at 100^{o} C for 24 hours prior to testing. The specimen was prepared using the dry pluviation method. This method involved depositing the sand particles into the mold in two lifts using a funnel and densifying using gentle tapping and vibration. The initial height of the specimen was 1.97 mm. After assembling the test cell components, the test cell was mounted on the stage of the beamline for scanning.

SMT and 3DXRD Scans

The SMT and 3DXRD scans were acquired at beamline 1-ID of the Advanced Photon Source (APS), Argonne National Laboratory (ANL), Illinois, USA. The C hutch of beamline 1-ID was initially designed to conduct 3DXRD experiments, and recently, SMT imaging capability was incorporated in the experiment setup (Figure 2). The test cell was mounted on a high precision positioning stage, which provided translation in x, y and z directions as well as rotation around the z-axis perpendicular to the incident beam direction (ω rotation). The SMT imaging system (scintillator and CCD camera) was mounted on a horizontal translation stage between the 2D panel diffraction detector and the test cell. (see Figure 2). The system was moved behind the test cell in line with the x-ray beam to collect attenuated x-ray for SMT scans. To prevent any damage to the 2D panel detector from diffracted x-rays while acquiring the SMT scans, a square metal plate with

a central hole was positioned between the test cell and SMT imaging system. The distance between the specimen and the imaging detector enabled obtaining a sufficient phase contrast on the sand particles in SMT images, which is necessary since, at high-energy x-rays, the x-ray absorption contrast would not be sufficient for clear, high resolution reconstructions.

SMT scans were acquired using 70.5 keV x-ray energy. 900 frames were collected by rotating the specimen at 0.2° angular increments over 180° at 0.65 second exposure time. The phase-contrast SMT scans contained a spatial resolution of 1 μm/pixel. The beam size was 1.6 mm (width) x 2.0 mm (height). A QImaging Retiga 4000R CCD camera (2048x2048 pixels) was used for the image collection.

3DXRD scans were acquired at the same energy as the SMT scan, which corresponds to a wavelength of 0.17586 Å. The scans were acquired at four different heights using a beam size of 0.5 mm x 1.0 mm (height x width), which provided a flat beam intensity evenly illuminating multiple sand particles per scan. The different heights assured that the acquired diffractograms contained evenly sampled and accurate information about the deformed lattice. The images of individual layers were acquired at 1° angular intervals (rotation interval, $\Delta\omega = 1°$) while rotating the specimen with constant speed from $\omega = 0°$ to $\omega = 180°$. Diffraction data was recorded using an amorphous silicon flat-panel detector (model GE Revolution 41RT) positioned at a horizontal distance of 1391.905 mm from the specimen stage. The detector dimensions were 410 mm x 410 mm (2048 x 2048 pixels), and the pixel size was 200 μm x 200 μm (Lee et al. 2008).

Initially, the SMT and 3DXRD scans were acquired consecutively before applying any load to the specimen. Then, 1D compression was applied at a constant displacement rate of 0.2 mm/min. The loading was paused when the desired load was reached, which was followed by a small load relaxation in the system. Therefore, the scans were performed after waiting for about 5 minutes

until the load relaxation rate diminished to a very small value. The actuator was held in position while acquiring the SMT and 3DXRD scans. This procedure was repeated for seven different load stages. The SMT scan for load stage 3 was skipped due to beamline time constraints.

Results

Specimen deformation under 1D compression

The load versus displacement relationship of the 1D compression experiment is depicted in Figure 3. The load increased as the compression progressed, however it slightly decreased when the loading was paused for scanning due to load relaxation. Relatively high magnitude load drops and oscillation emerged at high loads, which was shown to be caused by the fracture of silica sand particles within the assembly. The friction between the specimen and the acrylic mold increased as the compression progressed due to densification of specimen and tendency of particles to rearrange. Moreover, the fragments of fractured particles filled the void spaces between un-fractured particles, which resulted in denser packing and more particles in contact with the container walls. In addition, sand grains/fragments have a higher hardness than the walls of the acrylic mold and they penetrated the mold wall surface as compression progressed, which resulted in a gradual increase in the difference between the readings of the top and bottom load cells.

Figure 4 shows the axial cross sections of the SMT images at different load stages. These in situ 3D images permitted monitoring of the deformation behavior of the sand assembly and the evolution of particle fracture during axial compression. The initial unloaded stage is labeled as load stage 0 in Figure 4 which shows the arrangement of some sand particles in the middle vertical plane of the specimen. Since the specimen was densely packed, a few sand particles exhibited small rearrangement as the load increased during the first two load stages. The rearrangement was

not noticeable in the sequential images. To track the evolution of particle fracture in the specimen, the fracture mode (i.e., single/ multiple splitting, asperity damage, breakage of edge, progressive failure of one crack or multi-crack failure mode) of each sand particle was tracked throughout the experiment using SMT images. A sand particle is labeled as fractured if it experienced a major splitting into two or more fragments. The first particle fracture was observed between load stage 3 and load stage 4 (three particles fractured) and the number of fractured particles increased thereafter. 13 out of 35 sand particles did not exhibit any form of major fracture at the end of the experiment. The majority of the sand particle fractures occurred in particles close to the top loading platen which is in agreement with the observations reported in Cil and Alshibli (2014). This observation suggests that these particles are more prone to fracture due to relatively fewer contacts (i.e., less support provided by neighboring particles). Detailed analyses of particle fracture are provided in later Sections.

3DXRD Data Analysis

The incident monochromatic synchrotron x-ray beam was scattered on the orderly arranged atoms of a crystalline material. The diffracted x-ray beams obeyed Bragg's law:

$$2d_{hkl} \sin \theta_{hkl} = \lambda \tag{1}$$

where λ is the wavelength of the incident beam, θ_{hkl} is the angle of the incident beam to the lattice planes with spacing d_{hkl}. The subscript *hkl* denotes the lattice planes with Miller indices of *h*, *k*, and *l*. Consequently, diffracted beams originating from a crystal can be observed only in those directions that fulfill the Bragg condition (Eq. 1) and constructive interference happens determined by selection rules on Miller indices due to the crystal symmetry and the atomic form factors.

During the rotation of the specimen with a constant speed – as in this experiment– some of the crystallographic planes in the illuminated volume at some point will satisfy the Bragg condition and thus give rise to the diffracted intensity that can be acquired as spots on the detector image. Figure 5 shows an example raw image that contains sum of all the intensities acquired during a full scan (rotation over 180º), where the diffraction spots are organized along the so-called Debye-Scherrer rings. The position of each diffraction spot is defined by three specific angular coordinates (2θ, ω and η), which are used to determine the orientation of the corresponding set of lattice planes. 2θ is the angle between incident beam and diffracted beam, ω is the angular position of the rotation stage, and η is the azimuthal angle on the 2D panel detector and is measured relative to the vertical axis that coincides with the rotation axis. In diffraction data processing, the Bragg reflection is described by the reciprocal lattice vector ($\mathbf{g}_{hkl}$), which is perpendicular to the crystallographic planes with lattice spacing d_{hkl} and its magnitude is equal to the reciprocal of d_{hkl}. Therefore, $\left|\mathbf{g}_{hkl}\right|$ $(1/d_{hkl})$ is in direct correspondence with lattice strain. More information about the geometric principles of 3DXRD technique can be found in (Poulsen, 2004).

The first step in far-field diffraction data analysis is the calibration of the experimental setup, which was performed with the powder diffraction patterns of standard calibrants LaB_6 and CeO_2. The HEXRD open-source software package (HEXRD, 2014) was used to determine the calibration values. The calibration process provided the beam center, corrected specimen to detector distance, and the tilt of the detector. The raw diffraction images contained thousands of spots, but only a small portion of the data included useful diffraction peak spots. Therefore, the properties of diffraction spots must be identified and extracted from this large data set, which is also known as data reduction process. Peak searching was performed using DIGIgrain code that was developed by Kenesei (2012).

A correction algorithm was applied to each file that includes background correction, detector distortion, etc. For each full scan, all spots in the corrected files were consolidated into a single frame. DIGIgrain only identified the spots in pre-defined 2θ regions that were determined by examining the spot positions in raw diffraction patterns. Finally, a DIGIgrain peak search was applied to the corrected images and an iterative scheme was adopted to obtain optimum DIGIgrain parameters for this dataset. DIGIgrain output was saved in a simple text file that contained a list of identified peaks and their properties including center position, integrated intensity, and statistical descriptors. The center of mass position of the spots was computed in radial coordinates by DIGIgrain software. This approach eliminates radial error in peak position computation, which is important in strain analysis since the applied stress causes peaks shift in the radial direction.

The ImageD11 code of Wright (2005) was used to calculate g-vectors from indexed peak positions. Then, the GrainSpotter code (Schmidt, 2014) was used to index grains, which is the assignment of the measured g-vectors to the corresponding grains that they originate from. GrainSpotter provides a list of indexed grains that includes the center of mass position, orientation and the list of the diffraction spots assigned to a grain. Finally, the lattice strain was calculated with the help of a Matlab script written by the authors. The computation of the elastic strain tensor is based on the following simplified relationship: grain-averaged lattice strain is directly proportional to the 2θ shifts of reflections recorded in unloaded and loaded conditions. In this paper, the lattice strain derivation is explained briefly and further details can be found in Margulies, et al. (2002) and Alshibli, et al. (2013). The lattice strain expression can be derived by differentiating Bragg's law and expressed as (Margulies et al. 2002):

$$\varepsilon_{hkl} = \frac{d_0^{hkl} - d^{hkl}}{d_0^{hkl}} = cos\theta_0 \Delta\theta \tag{2}$$

where ε_{hkl} is the strain measured perpendicular to a particular (*hkl*) plane, d^{hkl} and d_0^{hkl} are the lattice spacings of (*hkl*) plane in loaded and initial conditions, respectively, and θ is the angle between the incoming beam and the scattering plane normal. The 2θ shifts of peak positions were evaluated by comparing the measured g-vectors in loaded and initial (unloaded) conditions. The change in g-vectors in each load stage was determined by comparing the distorted lattice measurements with respect to initial unloaded condition. The same grain was tracked through different load stages by comparing the indexed spots obtained by GrainSpotter and those identified in η-ω maps. Since the experiment was conducted by rotating the specimen over an angular range from ω = 0° to 180°, a particular set of planes that fulfill the Bragg condition gives rise to diffraction spots on the detector twice during the rotation. These spots are known as Friedel pairs and they are scattered from the crystallographic planes (*hkl*) and ($\bar{h}\bar{k}\bar{l}$) of the same grain (Ludwig et al. 2009; Moscicki et al. 2009). The diffraction angles and the magnitudes of diffraction vectors of Friedel pairs are the same. Therefore, the lattice strain calculations were performed using Friedel pairs to minimize the error in the diffraction data analysis. Further information about the formulation and details of the lattice strain computation can be found in Poulsen (2004) and Alshibli et al. (2013).

Lattice strain/stress results

Peaks were identified using the DIGIgrain program, and were sorted based on their grain of origin via GrainSpotter in each layer. The most challenging part of the diffraction data analysis was to match each indexed grain with the corresponding silica sand particle. Since the integrated intensity of each peak is directly proportional to the grain volume where it originates from, the integrated intensities of the peaks in the first ring (2θ = 2.36°) and third ring (2θ = 4.10°) were

calculated for each indexed grain and compared with the sand particle volume data that was obtained from SMT images. Similar to the 3DXRD scan layers, each SMT image was also divided into 4 layers, and an identification number was assigned to each particle (Figure 6). This matching process was repeated for each scan layer in all load stages. 34 out of 35 grains were indexed and tracked in consecutive load stages and were successfully matched with the corresponding sand particles in SMT images using this approach. Only Particle 31 could not be indexed in diffraction analysis, which likely stems from its small volume compared to other particles and possible defective crystal structure. The lattice strain measurements were then used to compute the corresponding lattice stress tensor of each sand particle assuming elastic stress-strain relationship following the same procedure described in Cil, et al. (2014). The elastic constants of quartz are reported by Heyliger, et al. (2003).

The global axial load versus the lattice strain relationships of 34 particles are displayed in Figures 7 through 12, and the evolution of corresponding principal stress-strain curves are showed in Figures 13 and 14. Since the sand specimen is composed of discrete particles, they may translate and rotate independent of each other when they are loaded globally. In the lattice strain calculation, all layers were analyzed simultaneously, which enabled identifying partially scanned grains in two different layers. If a particle appeared in two scans, the strain tensor of each fraction was computed and the particle strain was calculated by summing the strains of fractions together proportional to their volumes. In most of the cases, the tracking continued until the particle experienced a major fracture resulting in multiple small fragments and loss of reference crystal structure. If only a small portion of a particle is fractured (labeled as minor fracture in lattice strain plots) then the largest fragment of the fractured particle with close orientation was tracked if it was initially indexed. For each particle, all components of the lattice strain/stress tensor were computed and the three

principal strain versus principal stress values are reported in Figures 13 and 14. The major principal strain of most of the particles increased as the compression load increased. This was very evident during the initial load stage before the occurrence of initial fracture events. However, this trend was not observed in all particles due to rather complex particle-scale interactions within the granular assembly. It is critical to note that the computed lattice strain data corresponds to volume-averaged measurements, which means that the magnitude and direction of the lattice strain did not directly correlate with contact forces, but rather depend on particle characteristics (size and shape) and contact force properties (magnitude, direction and location). Some particles may be subjected to bending deformation, which leads the grain-averaged lattice strain to be close to zero. Depending on the combined effect of such parameters, a given contact force may induce significantly different lattice strain in two different particles within a granular assembly.

The principal strain values vary in a range between -0.9% and 0.26%, which is similar to the ranges of strain measurements reported by Alshibli et al. (2013). Also, it should be noted that the reported lattice strain values in fractured particles are the last measurements taken before fracture. Since the applied stress in a sand particle may change considerably during the loading increment when fracture took place, these last measurements cannot be considered as the failure strain or stress values. Hall and Wright (2014) reported lattice strain measurements between -0.5 - 0.15% for single crystal synthetic silica particles with almost spherical shape, but the applied global axial load increased up to 70 N and they did not report any particle fracture. The specimen diameter in this study is small and natural sand particles have inherent defects (flaws and crystal defects at which fracture can initiate) and sub angular-to-angular shape, which make them more prone to fracture.

Forces are transmitted through contact points between particles in granular materials. Each particle may have several contact points (Coordination Number, CN) and can be subjected to contact forces in multiple directions and magnitudes. The force transmission mechanism in particulate systems is very complex and difficult to analyze. Most particles in a granular assembly carry less than average contact force, and particles within force chains carry the majority of the axial load (Peters et al., 2005). As a result of this non-homogenous contact force network, the lattice strain of some particles increased as the axial load increased; however, the measured strain values in some particles are relatively small. Moreover, the rotation, translation, and fracture of individual sand particles during loading lead to rearrangement of neighboring particles and redistribution of the contact force network after particle fracture events. Therefore, observation will likely show variation and fluctuation in measured lattice strain values from particle to particle and from one load stage to the next as a result of changes in the magnitude, direction and number of contact forces on each particle (see Figures 7 through 12)

Particle fracture analyses

One observation made during the visual examination of the 3D SMT images was that some of the particle groups resembled nearly vertical columns of particles inside the cylindrical container and initial particle fracture events were observed in these particle columns. This suggests that some of the axial force was transmitted through these particles. Two particle groups that showed initial particle fractures during load stages 4 and 5 were selected to investigate the characteristics of particle fracture by visually tracking individual sand particles in SMT images collaborated with lattice strain and stress measurements. The orientation and arrangement of particles were examined using 3D renderings of sand particles that were generated from SMT

images. The Avizo Fire commercial image visualization software was used to process images. Since the absorption difference between air and particle phases is negligible in SMT images acquired at high x-ray energies, conventional threshold-based segmentation could not be implemented on these images. The sand particles were segmented via an image processing procedure similar to the one described in Druckrey and Alshibli (2016). The anisotropic diffusion filter was initially applied to the raw grayscale images to remove noise without blurring boundary contrast. The edges on particle boundaries were identified using Sobel filter. The particles were separated from the surrounding pore space, container, and platens using the watershed algorithm. The particles were then labelled one by one manually using the segmentation editor of Avizo Fire.

Two sand groups (labeled here as groups 1 and 2) and their evolution between load stages 0 and 7 are displayed in Figures 15 and 16, respectively. In addition, the CN of particles and the highest measured principal lattice strain before fracture are also added to Figures 15 and 16. The relative position of the selected particles within the specimen are highlighted in Figure 15a and Figure 16a. Three of the particles within group 1 fractured between load stages 3 and 4, which suggests that some portion of the axially transmitted load was carried by these particles. Group 1 continued to carry some of the axial load in load stage 5 despite the fracture of a few particles. It was observed that Particle 5 continued to disintegrate, and Particle 6 fractured during load stage 5 (see Figure 17). The relatively small specimen size also has an effect on progressive fragmentation of the same particles since forces will be redistributed and other grains will probably carry the load in a larger specimen size. In group 2, Particle 19 and Particle 30 fractured during load stage 5, as shown in Figure 18, and the measured major principal strain versus stress values initially increased for Particles 19, 22, 33 and 34 during compression, which demonstrates that some of the axial force was transmitted through group 2. The analysis was performed until load stage 6, since

several fragments from fractured particles filled the void space within the specimen, which made it difficult to identify produced fragments of tracked particles and contact structure in SMT images.

The fracture strength of a sand particle is influenced by several factors including mineralogy, crystal structure, CN, the direction and position of contact forces, particle size, particle orientation, particle morphology, and the number and distribution of flaws. It is not easy to measure contact forces between natural sand particles experimentally in 3D for many reasons including (i) a contact surface between two particles encompasses multi-points that may not lie on a plane; (ii) one may use grain-averaged lattice strain measurements such as the case for measurements reported in this paper to calculate average stress tensor within a particle assuming anisotropic elastic behavior of the sand grains (Alshibli et al. 2013). Linking the stress tensor to contact forces at particle boundaries needs few assumptions about the area of contact between two particles, and directions of tangent and normal vectors at the contact area.

In this paper, each particle was carefully examined in order to understand the causes of fracture by considering the effect of CN, lattice strain, particle shape and contact points of individual sand particles. The 3D renderings of fractured sand particles in groups 1 and 2 before and after fracture are displayed in Figures 17 and 18, respectively. Particle 9 is located at the top corner of the specimen and has 5 contact points (CN = 5). The CN did not change from load stage 0 until fracture (the top plate, the mold wall in the lateral direction, and Particles 8, 13 and 19). The shape of Particle 9 can be defined as sub-rounded. The fracture likely resulted from the contact forces applied by the top loading platen and Particle 8 below it. Particle 5 is an elongated particle with CN = 6. Although there are multiple contacts, the crack propagated along a slightly slanted vertical plane that connects particle contacts above and below it. Since the particle is elongated in the horizontal direction, it is vulnerable to vertical applied forces. Therefore, the orientation and

shape of Particle 5 may be important factors in the occurrence of fracture. Similar fracture modes were observed in Particles 6, 10, 19 and 30 (see Figures 17 and 18). These 3D images demonstrate that all the particles fractured via splitting into two fragments, and the cracks formed along the plane that connected the contact points. Although other particles in groups 1 and 2 had similar CN (see Figures 15 and 16), they did not experience fracture, which indicates that the coordination number is not the only parameter determining initial particle fractures in this sand assembly. The influence of a heterogeneous contact network should be to characterize the onset of particle fracture.

The evolution and magnitude of lattice principal strains versus principal stresses are other useful measurements to understand the causes of fracture. The principal strain versus principal stress increased in Particles 6, 8, 9, 10, and 14 in group 1, and in Particles 19, 22, 33 and 34 within group 2, which also confirms that these sand groups carried a portion of the increasing global load from the beginning of the experiment. Some sand particles experienced higher principal strain versus principal stress values when compared to the fractured particles, however they did not fracture. Therefore, other factors such as the direction and position of contact points, particle flaws and shape have to be considered in fracture analysis. 3D renderings of sand particles before and after fracture (Figures 17 and 18) demonstrated that a small fragment generally splits from the parent sand particle in all cases. Due to the irregular shape of sand particles, a portion of the particle become vulnerable to fracture if contact forces act along these parts. The fracture of three particles at a relatively small load (load stage 4 = 18.5 N) also points to the considerable role of stress localization at these weak regions (small cross-section of a particle and/or portions with sharp corners). As a result, only Particles 5, 9 and 10 in group 1 fractured at load stage 4, and Particles 19 and 30 in group 2 fractured at load stage 5, even though some other particles in these

groups have smaller CN and experienced higher strains. It can be concluded that CN is not a main predictive parameter for the initial particle fractures in this dataset. On the other hand, the position of contacts and particle shape as well as the magnitude of contact forces all play a significant role in the occurrence of particle fracture in the sand assembly. All particle edge breakages in Figures 17 and 18, and particle fractures observed in relatively small principal strain values in some particles support this hypothesis. One of the main conclusions reached from this analysis is that although a high contact force causes a stress concentration around the contact point, its influence on particle-averaged lattice strain/stress might be small. Therefore, contact properties and particle characteristics have a combined effect on the deformation and fracture of particles in this sand assembly.

Conclusions

SMT and 3DXRD techniques were successfully employed to examine lattice strain evolution and fracture of natural Ottawa sand particles. The volume-averaged lattice strains of individual natural sand particles within an assembly were measured using 3DXRD and then used to compute the corresponding lattice stress tensor of each particle. The evolution of the lattice strain tensor as a function of global applied axial load was calculated using the far-field diffraction data acquired at four different scan layers. The lattice strain versus principal stress analyses showed that the major principal strain versus principal stress value increased within most of the particles as the compression load increased until the onset of particle fracture, which resulted in reorganization of particles and variations in the results. The lattice strain values of some sand particles were relatively small, which indicates that these particles carry very small loads due to the non-homogenous contact force network in granular materials. The measured lattice strain values vary

considerably from one particle to another due to several factors including the number and position of contacts, particle shape and size, and the orientation of the particle.

The evolution of particle fracture was also investigated using 3D SMT images. Two sand particle groups were aligned in a nearly vertical direction. The first fractured particles were identified and examined in detail. After initial particle fractures, these groups continued to carry a portion of the axial load. The cracks in fractured sand particles generally extend along the plane that connects the two contact points of the particle with the neighbor particles and this plane is more or less parallel to the axial load direction. In most cases, particles initially split into two or three fragments. The produced fragments then experienced further breakage as they continue to carry load. Micro-scale fracture analysis revealed that the position of contact and particle shape played a major role in the occurrence of particle fracture, and CN is not the main predictive parameter for the initial particle fractures in this dataset. This experimental analysis revealed that 3D high-resolution SMT images acquired during the deformation of sand assembly and lattice strain measurements provided unique 3D measurements to gain insight into the fracture behavior of individual sand particles at the particle-level non-destructively. These micro-scale measurements demonstrate the great potential of these techniques to better understand and model the fundamental behavior of granular materials.

Acknowledgments

This material is based on work supported by the National Science Foundation under Grant No. CMMI- 1362510. Any opinions, findings, and conclusions or recommendations expressed in this material are those of the authors and do not necessarily reflect the views of the National Science Foundation. The SMT and 3DXRD images were collected using Beamline 1-ID at

Argonne Photon Source (APS), Argonne National Laboratory. Use of the Advanced Photon Source, an Office of Science User Facility operated for the U.S. Department of Energy (DOE) Office of Science by Argonne National Laboratory, was supported by the U.S. DOE under Contract No. DE-AC02-06CH11357. The authors thank Karen Lee and Zachary Panczer for help in digitizing some of the SMT images. The ODF/PF package for Matlab developed at Cornell University was used for this work (http://anisotropy.mae.cornell.edu).

References

Alshibli, K., Cil, M. B., Kenesei, P., and Lienert, U. (2013). "Strain tensor determination of compressed individual silica sand particles using high-energy synchrotron diffraction." *Granular Matter*, 15(5), 517-530.

Andò, E., Hall, S., Viggiani, G., Desrues, J., and Bésuelle, P. (2012). "Grain-scale experimental investigation of localised deformation in sand: a discrete particle tracking approach." *Acta Geotech.*, 7(1), 1-13.

Andrade, J. E., and Borja, R. I. (2006). "Capturing strain localization in dense sands with random density." *Int J Numer Meth Eng*, 67(11), 1531-1564.

Cil, M. B., Alshibli, K., Kenesei, P., and Lienert, U. (2014). "Combined high-energy synchrotron X-ray diffraction and computed tomography to characterize constitutive behavior of silica sand." *Nuclear Instruments and Methods in Physics Research Section B: Beam Interactions with Materials and Atoms*, 324(0), 11-16.

Cil, M. B., and Alshibli, K. A. (2014). "3D evolution of sand fracture under 1D compression." *Geotechnique*, 351-364.

Druckrey, A. M., and Alshibli, K. A. (2014). "3D Behavior of Sand Particles Using X-Ray Synchrotron Micro-Tomography." *Geo-Congress 2014 Technical Papers*, 2814-2821.

Druckrey, A. M., and Alshibli, K. A. (2016). "3D finite element modeling of sand particle fracture based on in situ X- Ray synchrotron imaging." *International Journal for Numerical and Analytical Methods in Geomechanics*, 40(1), 105-116.

Fonseca, J., O'Sullivan, C., Coop, M. R., and Lee, P. D. (2012). "Non-invasive characterization of particle morphology of natural sands." *Soils Found*, 52(4), 712-722.

Hall, S., and Wright, J. (2014). "Characterisation of 3D force transmission in real granular media." *16th International Conference on Experimental MEchanics*Cambridge, United Kingdom.

Hall, S., Wright, J., Pirling, T., Andò, E., Hughes, D., and Viggiani, G. (2011). "Can intergranular force transmission be identified in sand?" *Granular Matter*, 13(3), 251-254.

Hall, S. A., Bornert, M., Desrues, J., Pannier, Y., Lenoir, N., Viggiani, G., and Besuelle, P. (2010). "Discrete and continuum analysis of localised deformation in sand using X-ray mu CT and volumetric digital image correlation." *Geotechnique*, 60(5), 315-322.

Hall, S. A., and Wright, J. (2015). "Three-dimensional experimental granular mechanics." *Geotech Lett*, 5(4), 236-242.

Hasan, A., and Alshibli, K. (2012). "Three dimensional fabric evolution of sheared sand." *Granular Matter*, 14(4), 469-482.

HEXRD (2014). <https://github.com/praxes/hexrd>. (accessed October 10, 2014).

Heyliger, P., Ledbetter, H., and Kim, S. (2003). "Elastic constants of natural quartz." *The Journal of the Acoustical Society of America*, 114(2), 644-650.

Kenesei, P. (2012). "DIGIgrain." < http://sourceforge.net/apps/trac/digigrain/wiki>.

Lee, J. H., Aydiner, C. C., Almer, J., Bernier, J., Chapman, K. W., Chupas, P. J., Haeffner, D., Kump, K., Lee, P. L., Lienert, U., Miceli, A., and Vera, G. (2008). "Synchrotron applications of an amorphous silicon flat-panel detector." *Journal of Synchrotron Radiation*, 15(5), 477-488.

Lenoir, N., Bornert, M., Desrues, J., Bésuelle, P., and Viggiani, G. (2007). "Volumetric Digital Image Correlation Applied to X-ray Microtomography Images from Triaxial Compression Tests on Argillaceous Rock." *Strain*, 43(3), 193-205.

Ludwig, W., Reischig, P., King, A., Herbig, M., Lauridsen, E. M., Johnson, G., Marrow, T. J., and Buffiere, J. Y. (2009). "Three-dimensional grain mapping by x-ray diffraction contrast tomography and the use of Friedel pairs in diffraction data analysis." *Review of Scientific Instruments*, 80(3), 033905-033909.

Manzari, M. T., and Dafalias, Y. F. (1997). "A critical state two-surface plasticity model for sands." *Geotechnique*, 47(2), 255-272.

Margulies, L., Lorentzen, T., Poulsen, H. F., and Leffers, T. (2002). "Strain tensor development in a single grain in the bulk of a polycrystal under loading." *Acta Mater*, 50(7), 1771-1779.

Moscicki, M., Kenesei, P., Wright, J., Pinto, H., Lippmann, T., Borbely, A., and Pyzalla, A. R. (2009). "Friedel-pair based indexing method for characterization of single grains with hard X-rays." *Mat Sci Eng a-Struct*, 524(1-2), 64-68.

Penumadu, D., Dutta, A. K., Luo, X., and Thomas, K. G. (2009). "Nano and neutron science applications for geomechanics." *Ksce J Civ Eng*, 13(4), 233-242.

Peters, J. F., Muthuswamy, M., Wibowo, J., and Tordesillas, A. (2005). "Characterization of force chains in granular material." *Physical Review E*, 72(4), 041307.

Poulsen, H. F. (2004). *Three-dimensional X-ray diffraction microscopy: mapping polycrystals and their dynamics*, Springer.

Schmidt, S. (2014). "GrainSpotter: a fast and robust polycrystalline indexing algorithm." *Journal of Applied Crystallography*, 47(1), 276-284.

Viggiani, G., Takano, D., and Andò, E. (2014). "Laboratory X-ray Tomography: A Valuable Experimental Tool for Revealing Processes in Soils." *Geotech Test J*, 35(1), 66-71.

Wensrich, C. M., Kisi, E. H., Luzin, V., Garbe, U., Kirstein, O., Smith, A. L., and Zhang, J. F. (2014). "Force chains in monodisperse spherical particle assemblies: Three-dimensional measurements using neutrons." *Physical Review E*, 90(4), 042203.

Wright, J. (2005). "*ImageD11*." <http://sourceforge.net/apps/trac/fable/wiki/imaged11>.

FIGURE CAPTIONS

Figure 1. Schematic of the 1D compression test cell.

Figure 2. Experimental setup for 3DXRD and SMT measurements at 1-ID beamline of APS.

Figure 3. Global axial load/stress versus displacement/strain relationship of 1D compression test on sand specimen.

Figure 4. Axial slices extracted from the SMT images of the specimen (at the center) at multiple load stages (specimen diameter = ~ 1 mm).

Figure 5. A typical raw 3DXRD diffraction pattern of F-75 Ottawa sand, which is the sum of intensities acquired during a full scan.

Figure 6. Assigned identification numbers for sand particles in SMT image analysis.

Figure 7. Evolution of principal strain measurements for (a) Particle 1; (b) Particle 2; (c) Particle 3; (d) Particle 4; (e) Particle 5; and (f) Particle 6.

Figure 8. Evolution of principal strain measurements for (a) Particle 7; (b) Particle 8; (c) Particle 9; (d) Particle 10; (e) Particle 11; and (f) Particle 12.

Figure 9. Evolution of principal strain measurements for (a) Particle 13; (b) Particle 14; (c) Particle 15; (d) Particle 16; (e) Particle 17; and (f) Particle 18.

Figure 10. Evolution of principal strain measurements for (a) Particle 19; (b) Particle 20; (c) Particle 21; (d) Particle 22; (e) Particle 23; and (f) Particle 24.

Figure 11. Evolution of principal strain measurements for (a) Particle 25; (b) Particle 26; (c) Particle 27; (d) Particle 28; (e) Particle 29; and (f) Particle 30.

Figure 12. Evolution of principal strain measurements for (a) Particle 32; (b) Particle 33; (c) Particle 34; (d) Particle 35.

Figure 13. Evolution of the principal components of lattice stress-strain tensors of Particles 1-17 and stress triads showing the principal lattice stress components at principal stress directions at load stage 4. Each arm in stress triads is color coded for principal stress values based on the color bar.

Figure 14. Evolution of the principal components of lattice stress-strain tensors of Particles 18-35 (expect Particle 31) and stress triads showing the principal lattice stress components at principal stress directions at load stage 4. Each arm in stress triads is color coded for principal stress values based on the color bar.

Figure 1

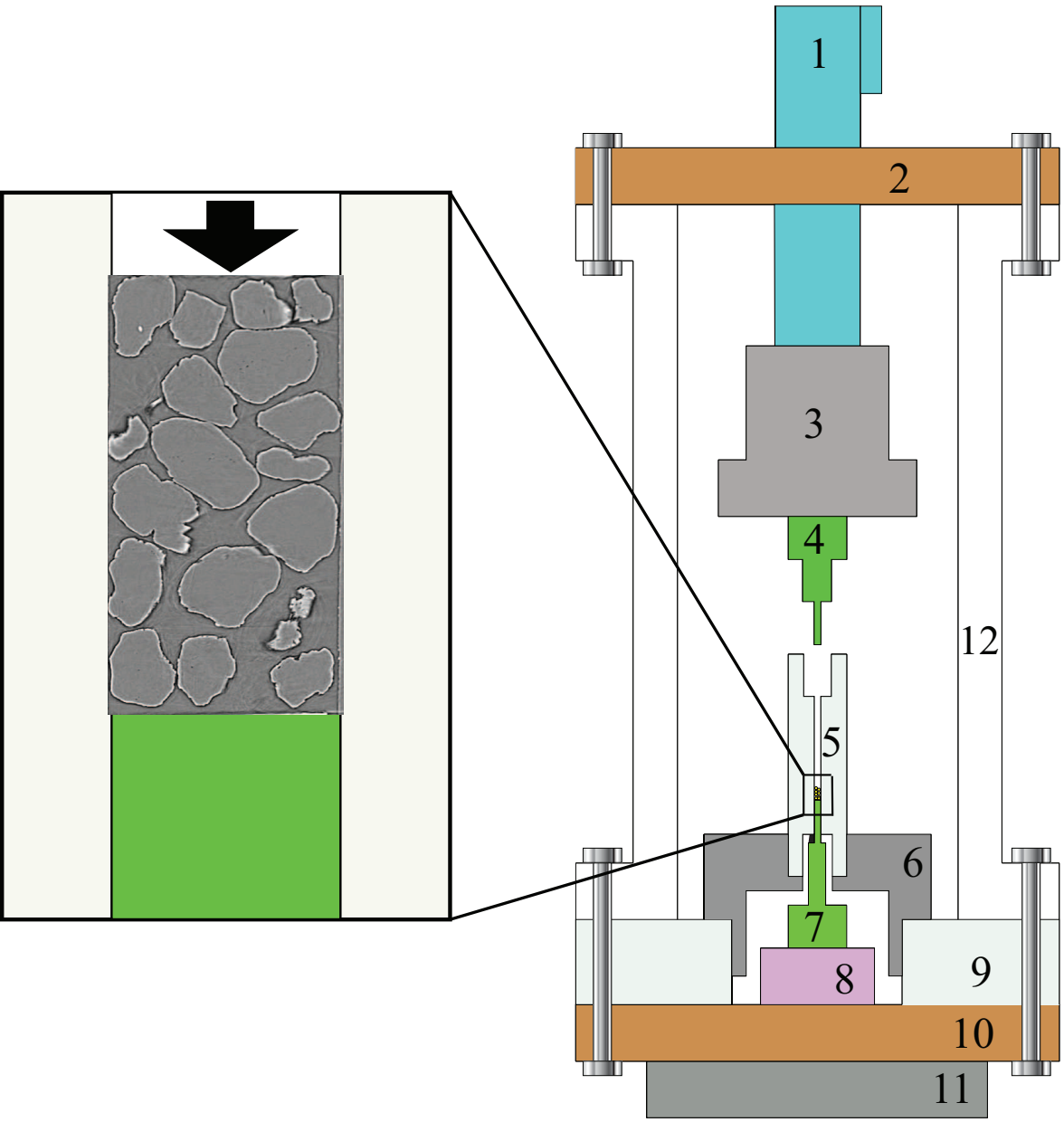

1: Stepper motor to apply axial loading
2: Top cell plate
3: Top load cell
4: Top loading plate
5: Acrylic mold with sand particles
6: Aluminum spacer
7: Bottom loading plate
8: Bottom load cell
9: Acrylic spacer
10: Bottom cell plate
11: Cell-stage connection plate
12: Acrylic chamber

Figure 2

Click here to download Figure
Figure_2.pdf

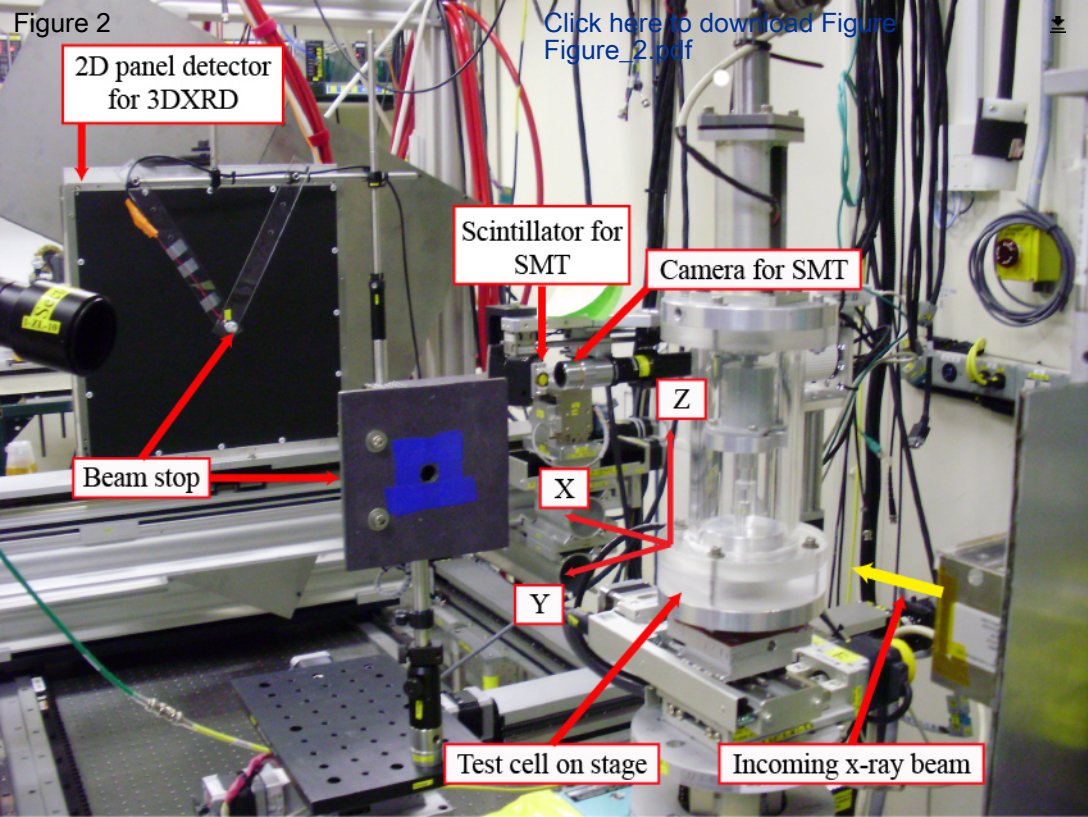

Figure 3

Click here to download Figure Fig_3.eps

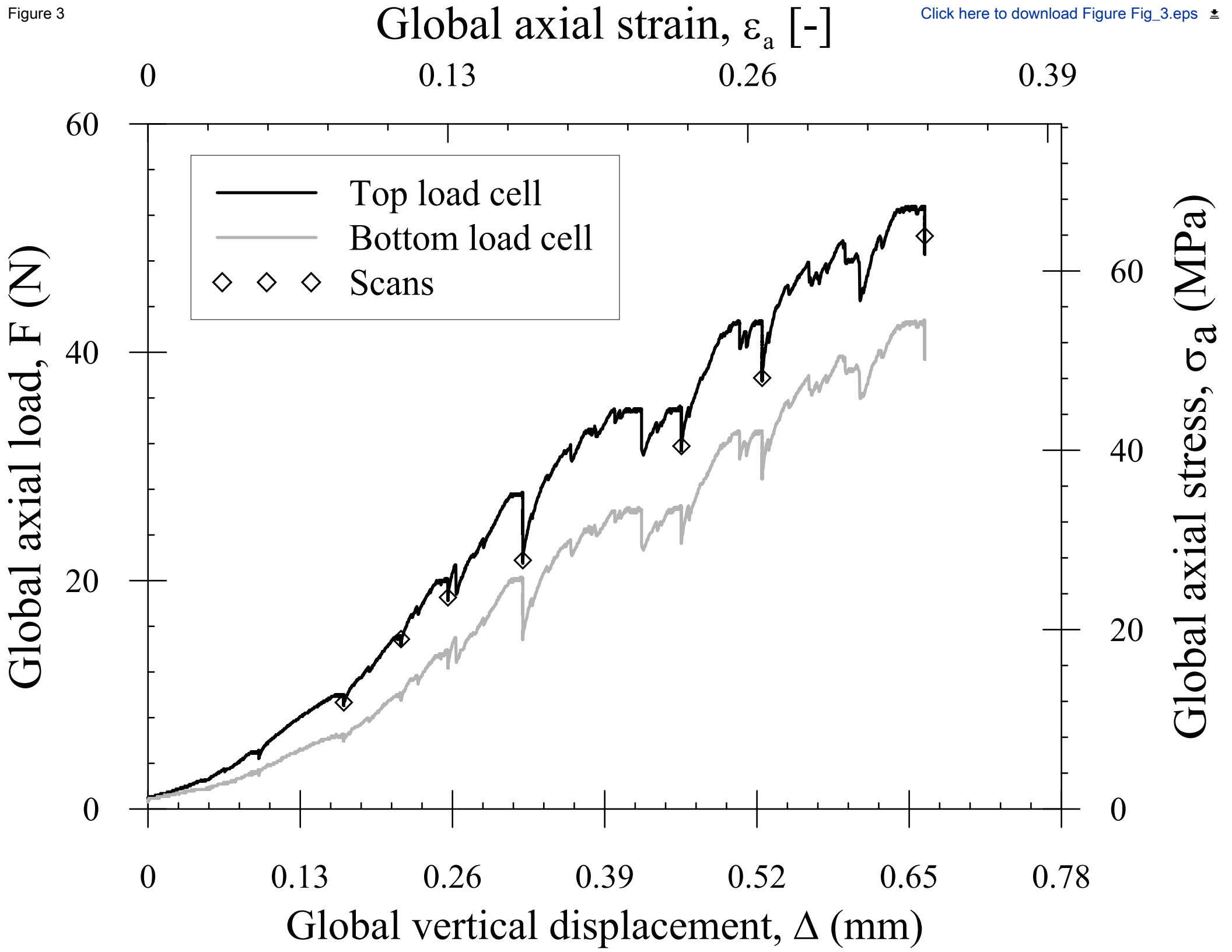

Figure 4

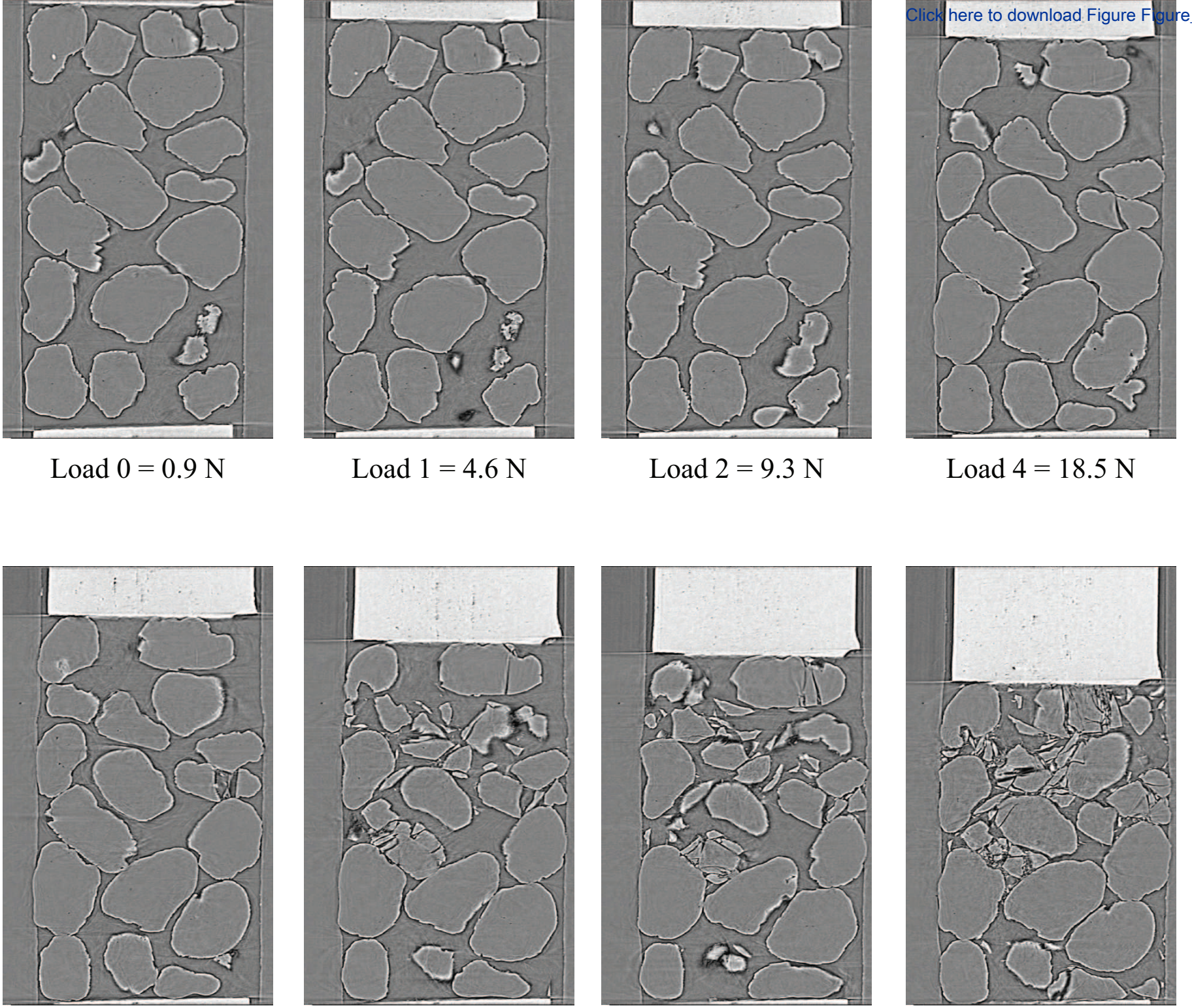

Click here to download Figure Figure_5.pdf

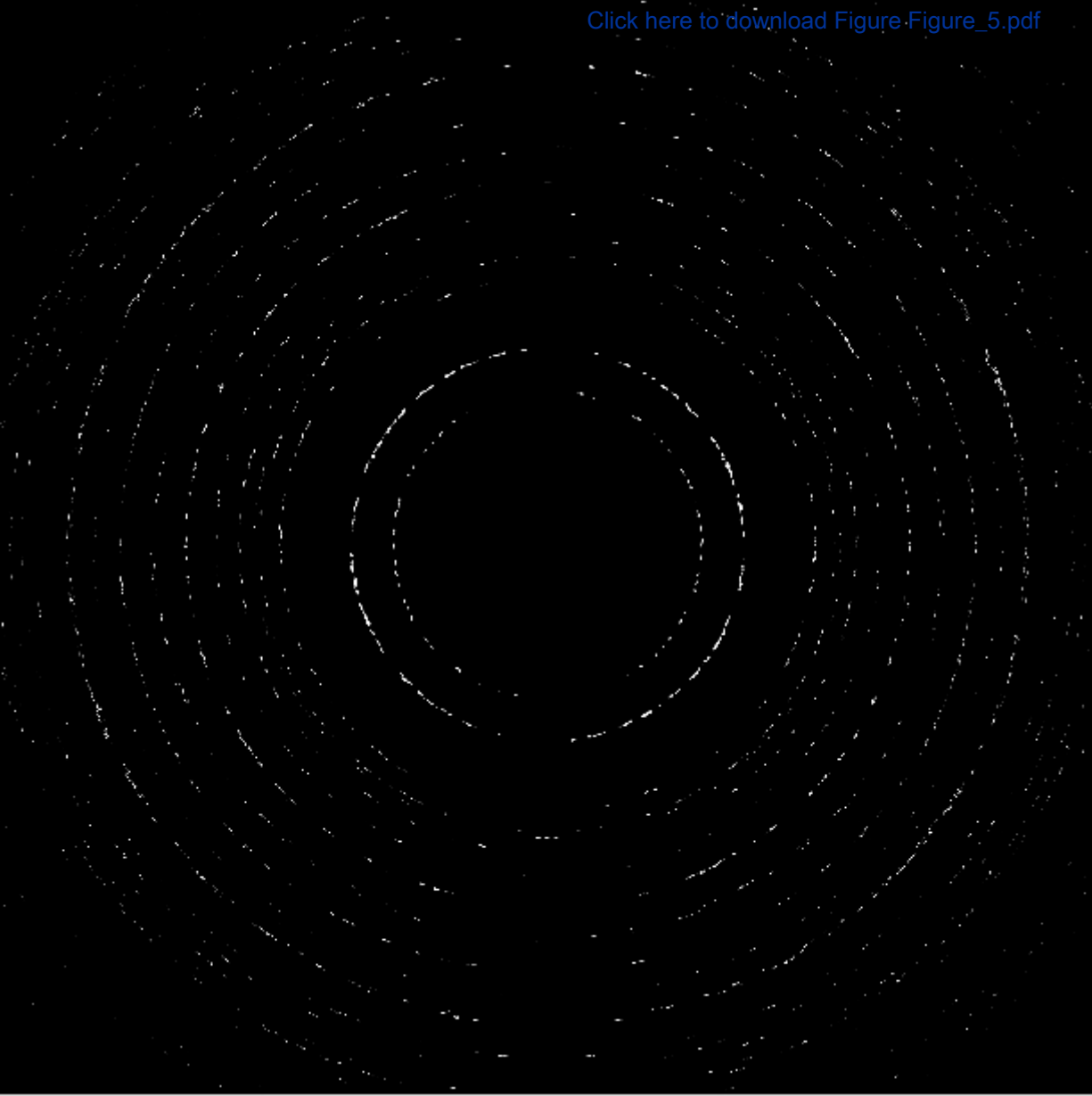

Figure 6

Click here to download Figure Figure_6.eps

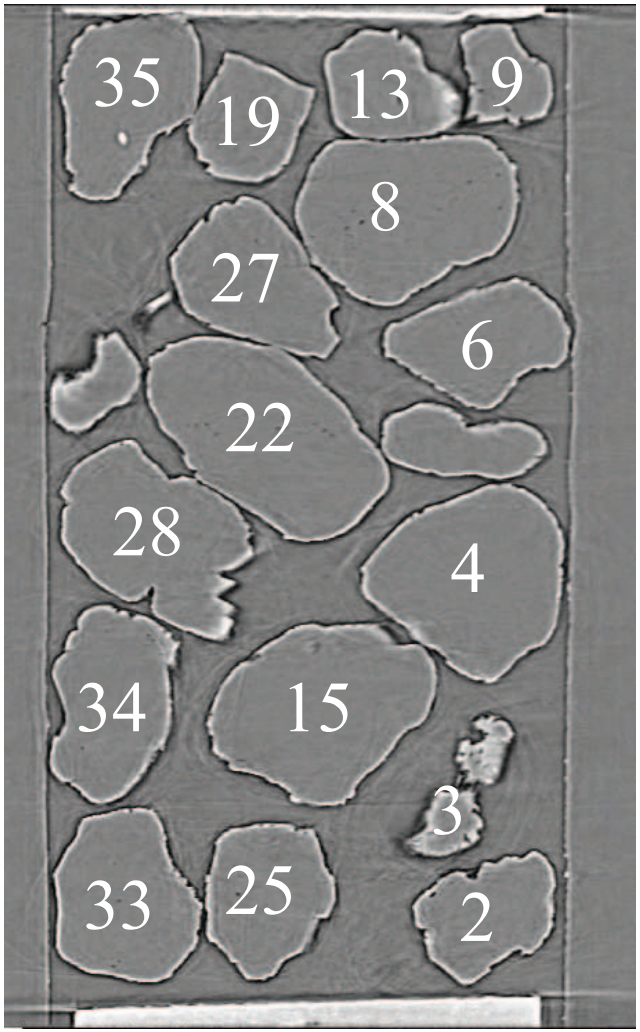

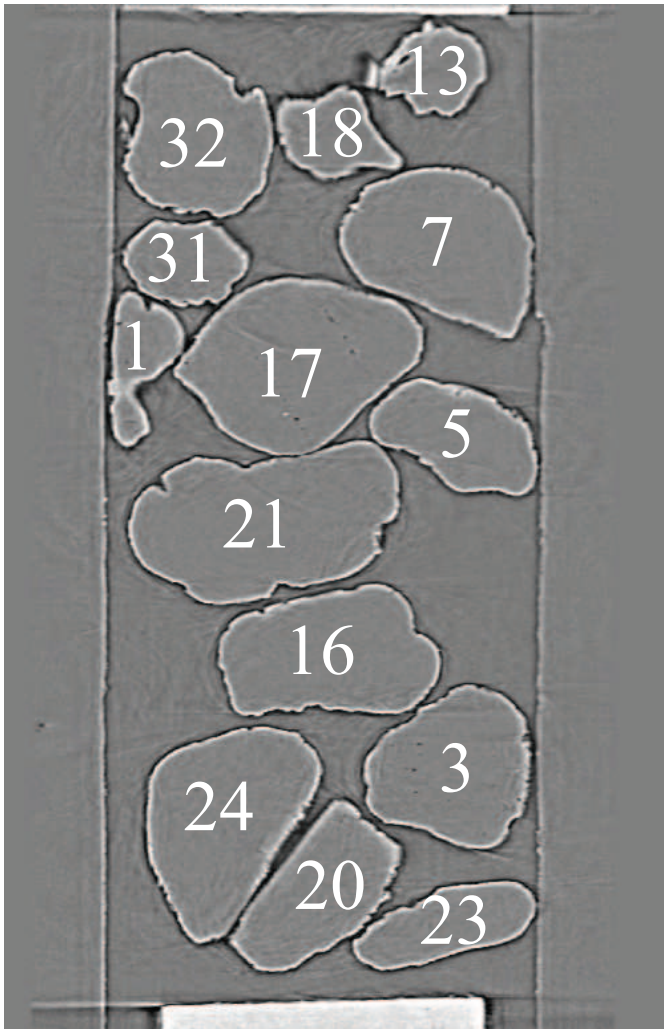

Figure 7

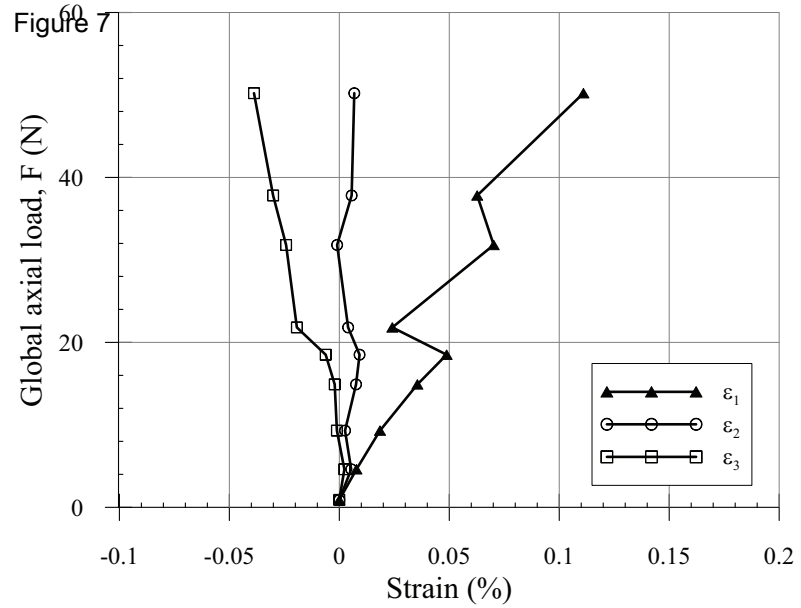

(a)

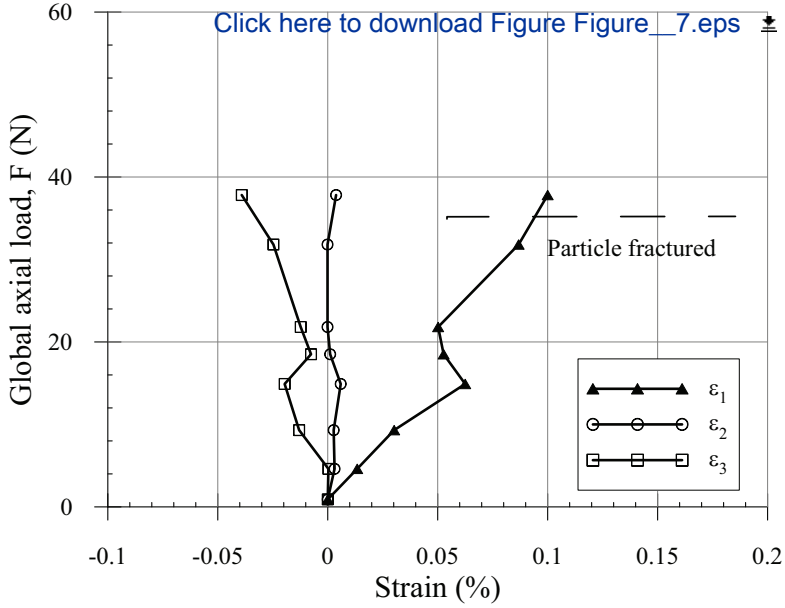

(b)

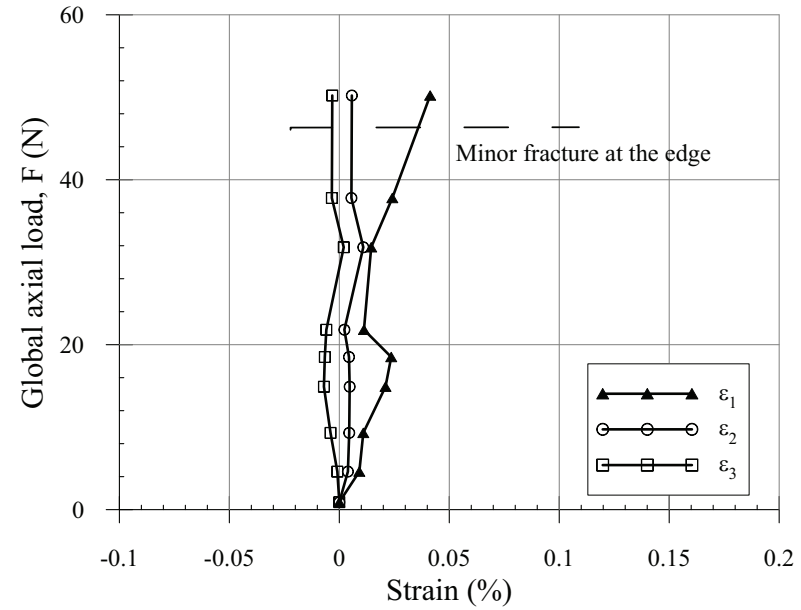

(c)

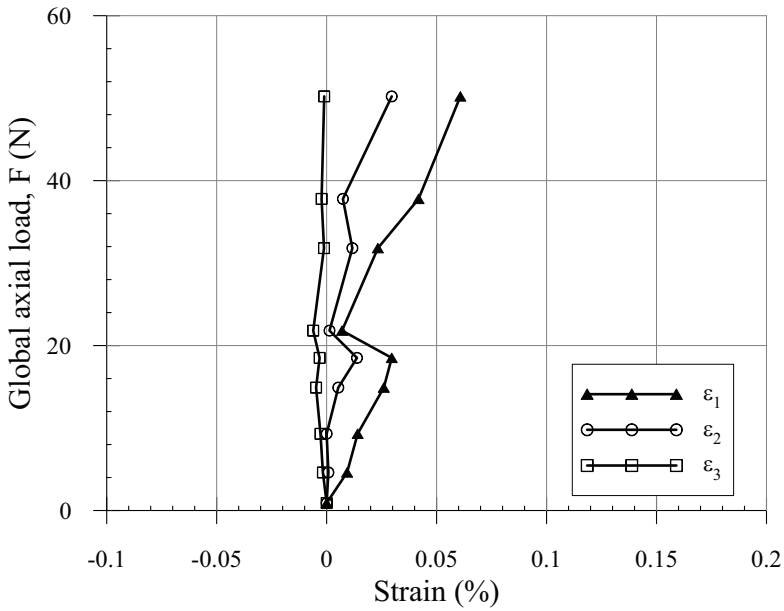

(d)

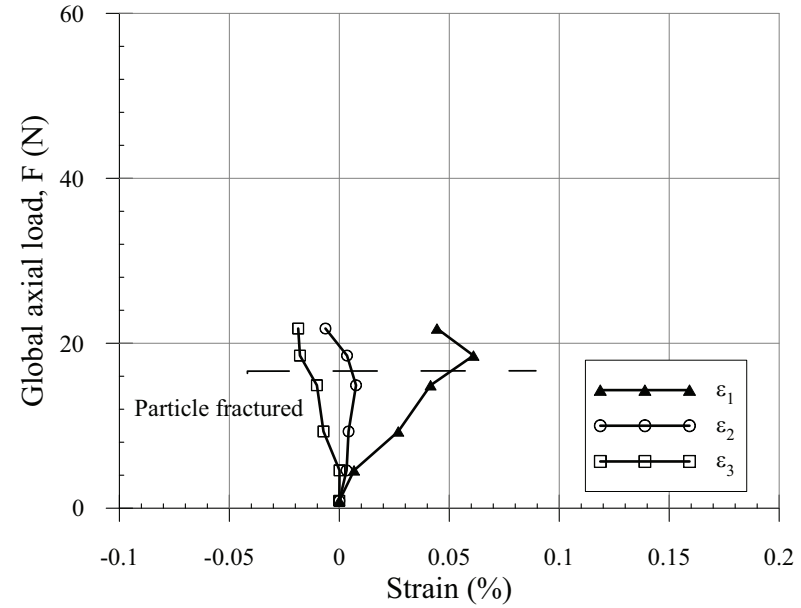

(e)

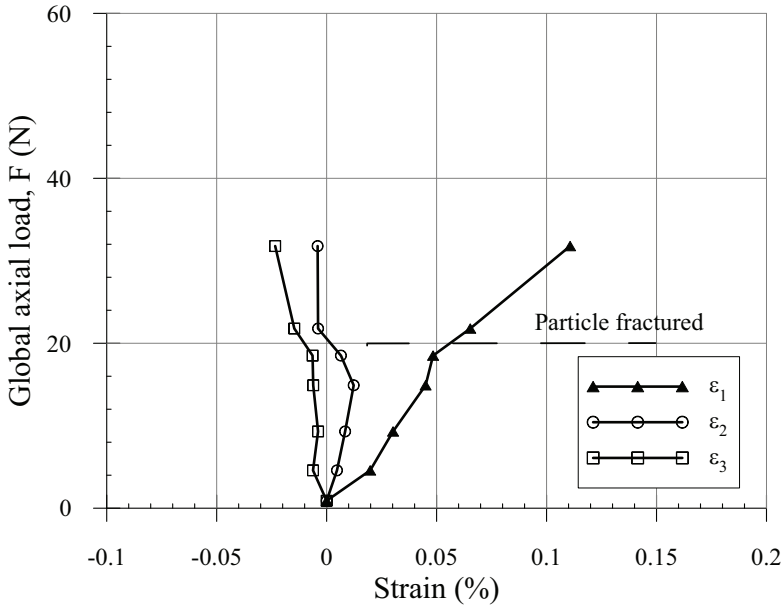

(f)

Figure 8

Click here to download Figure Figure__8.eps

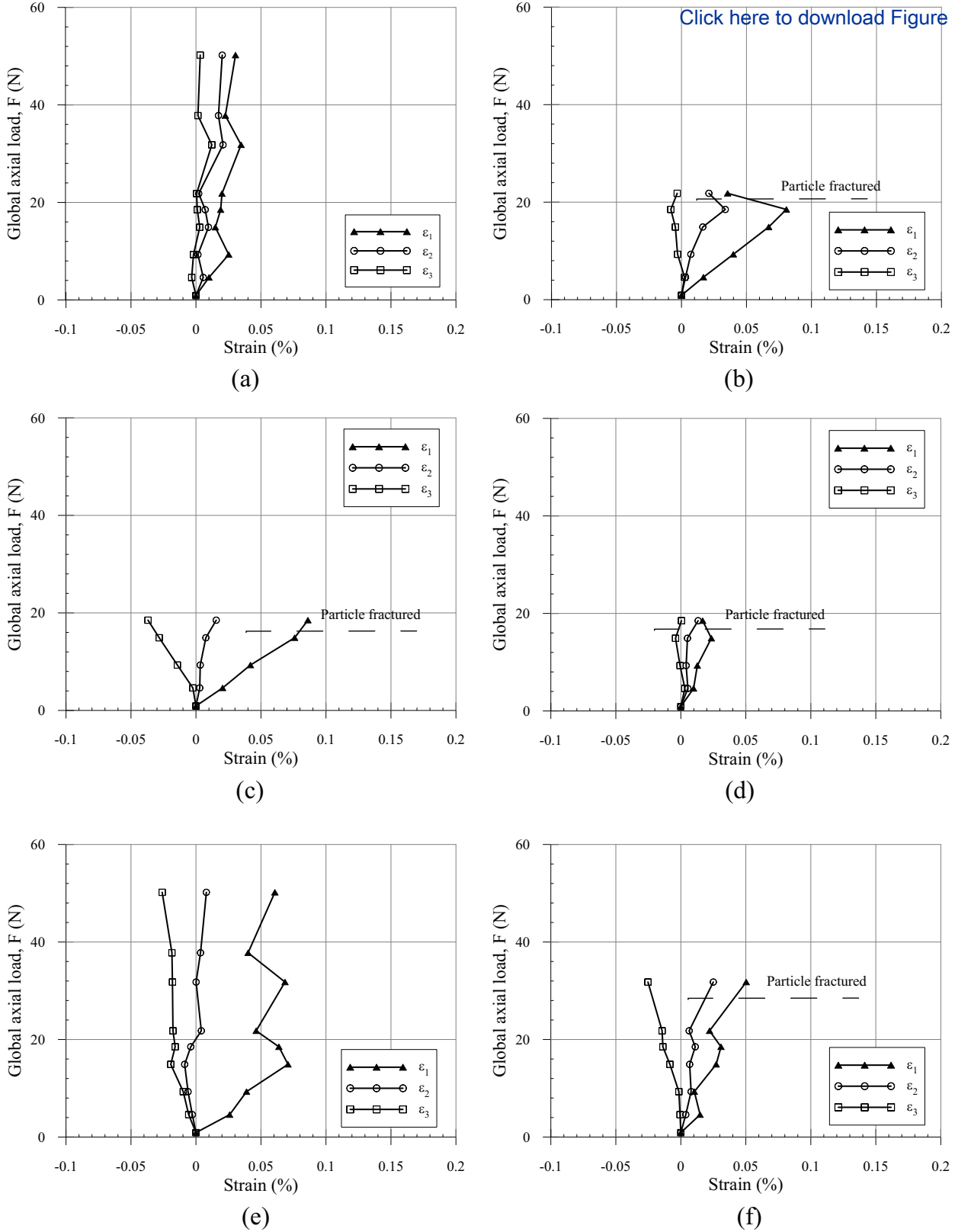

Figure 9

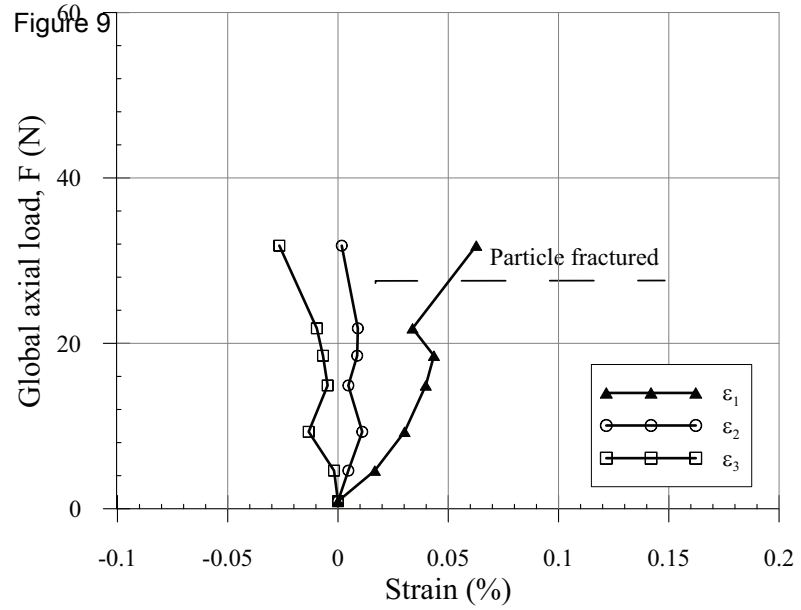

(a)

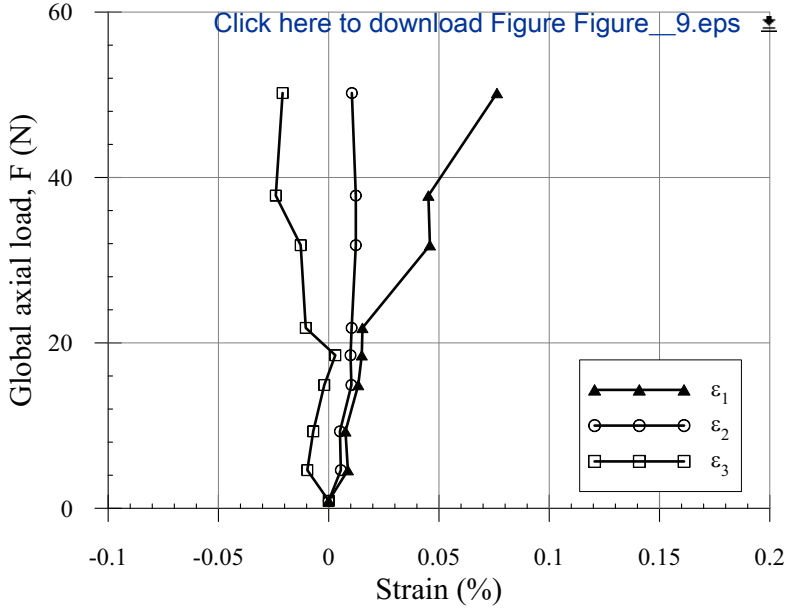

(b)

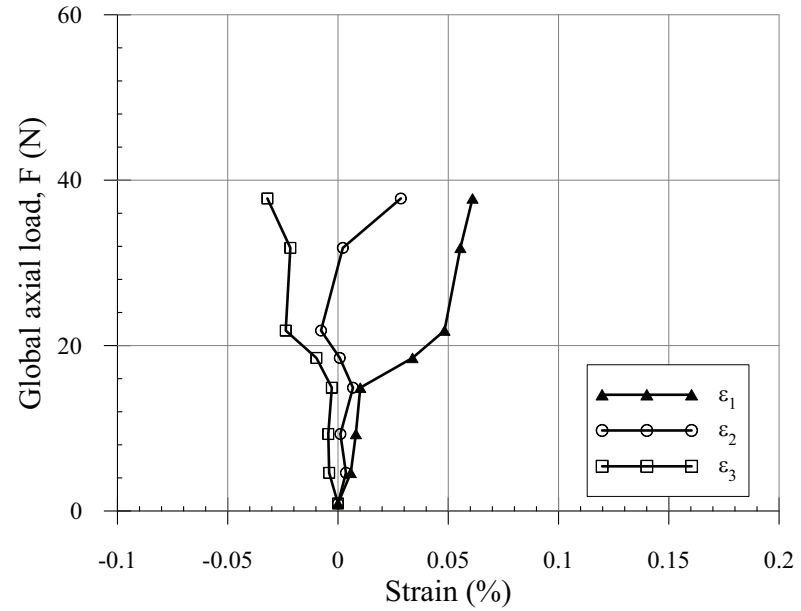

(c)

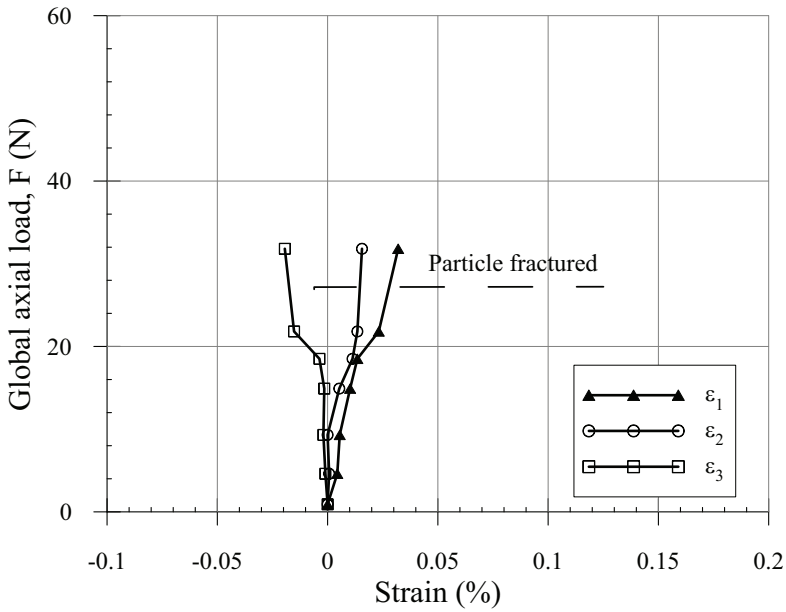

(d)

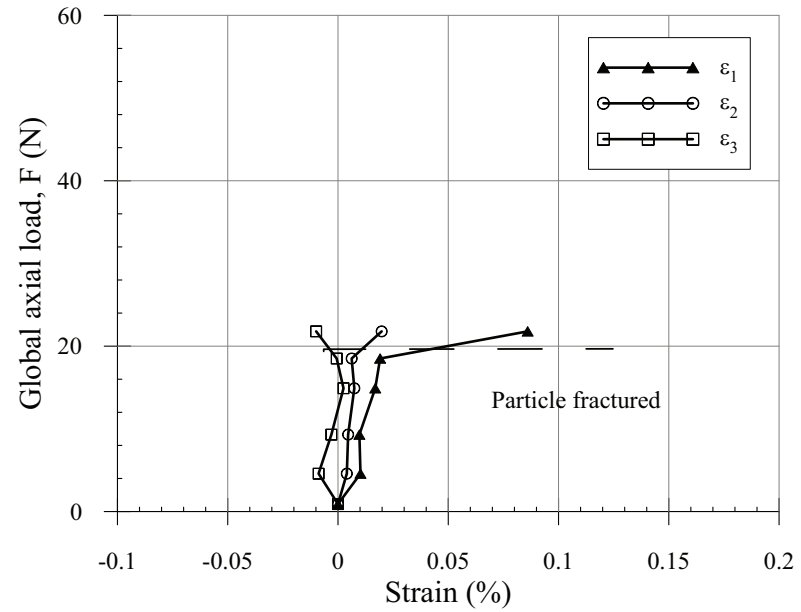

(e)

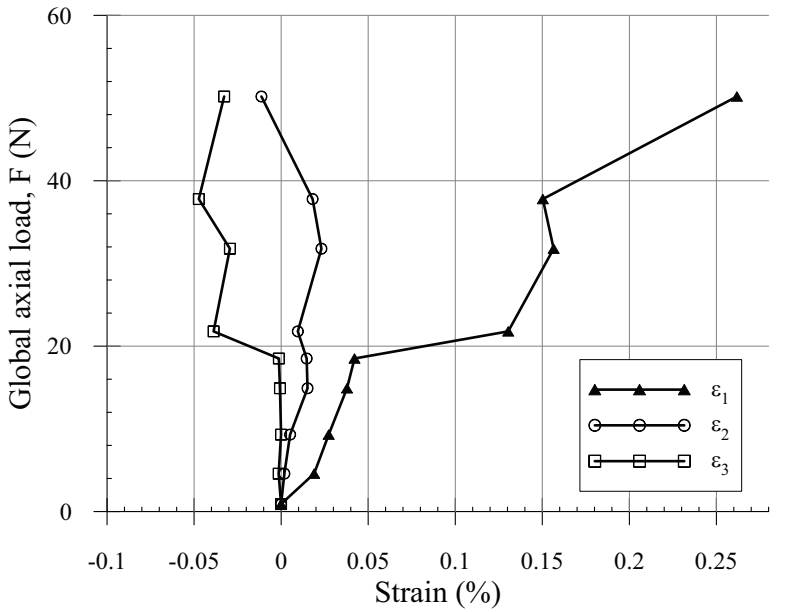

(f)

Figure 10

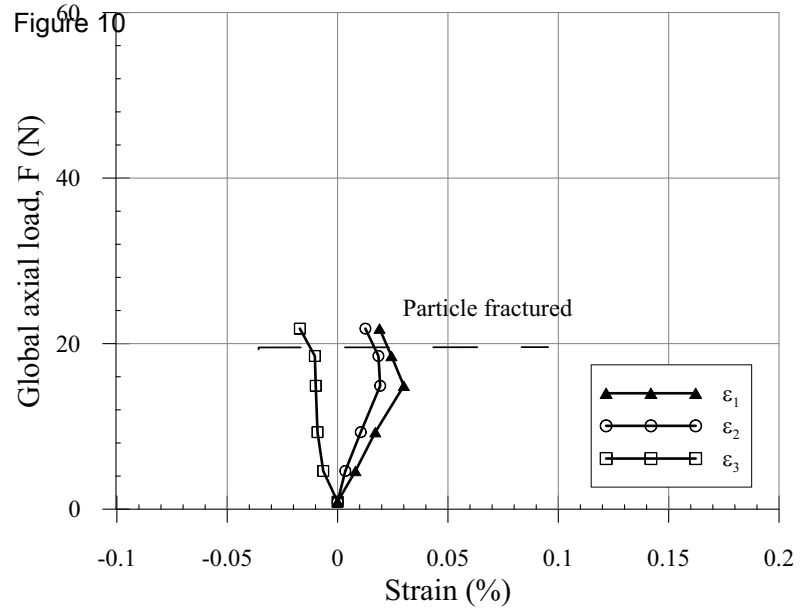

(a)

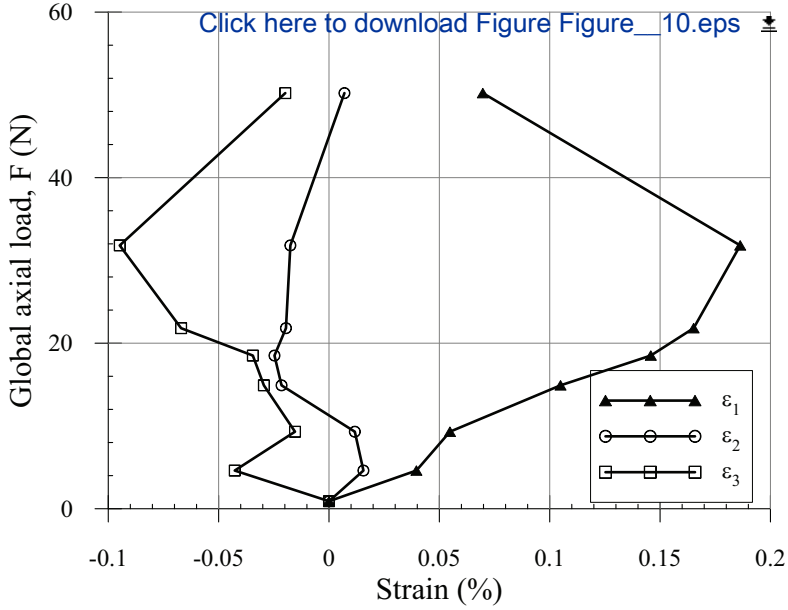

(b)

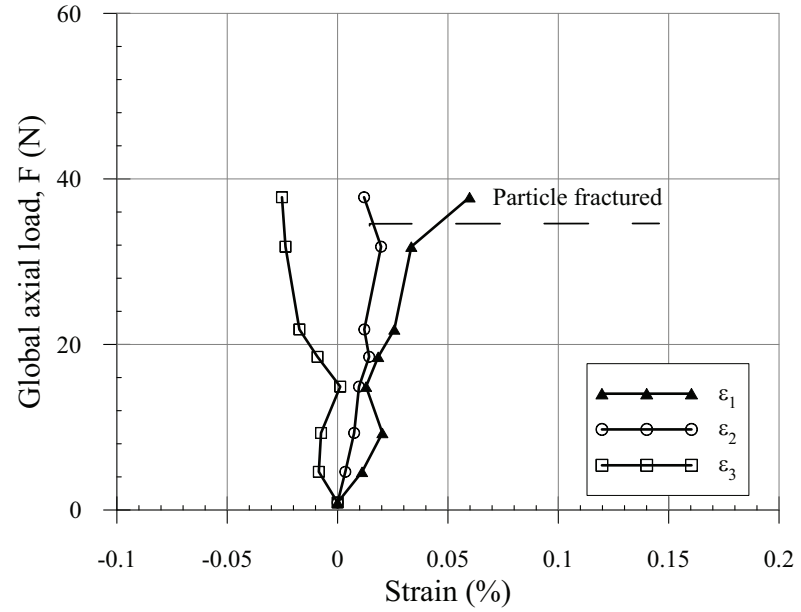

(c)

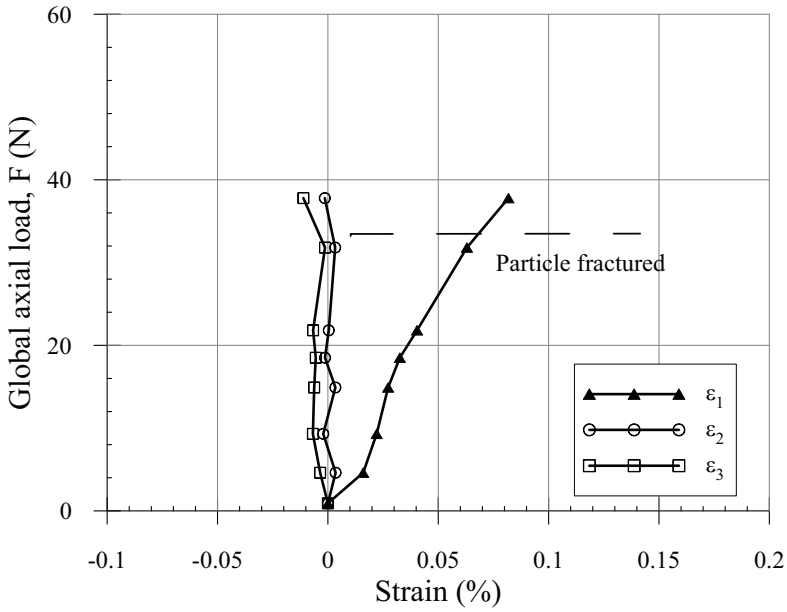

(d)

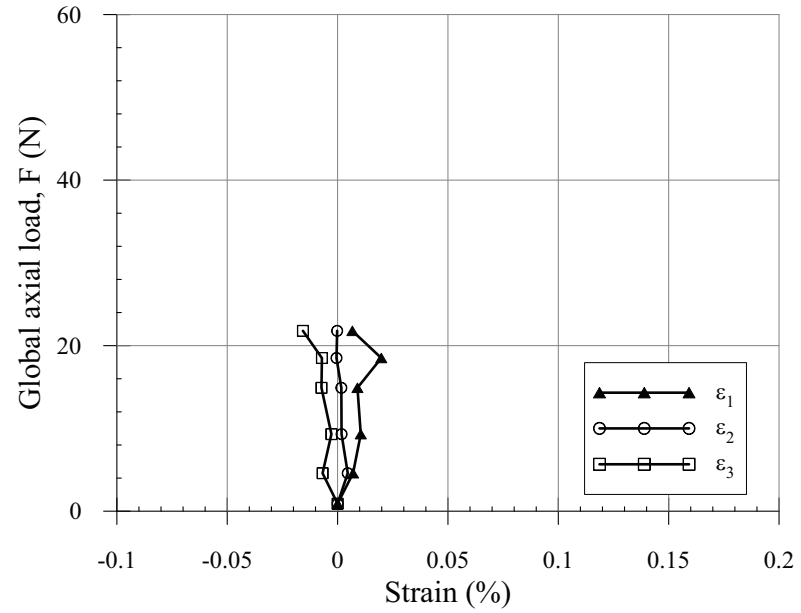

(e)

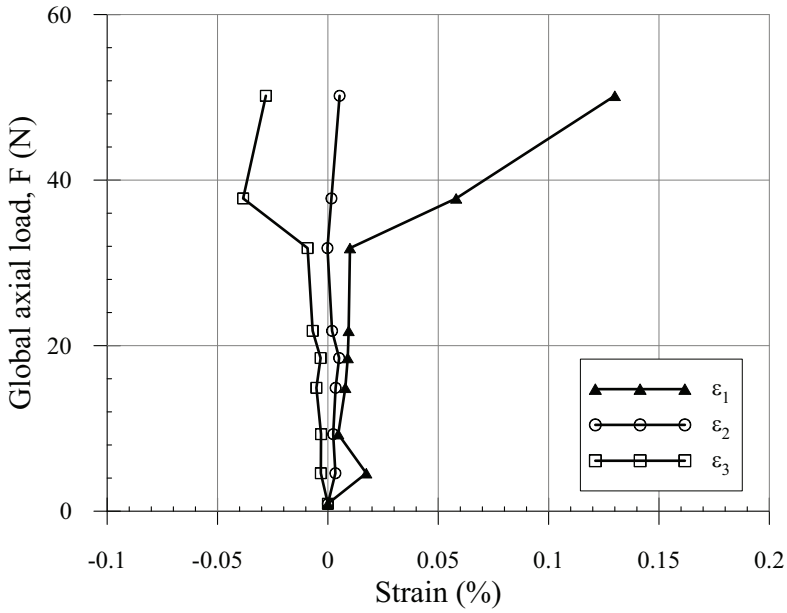

(f)

Figure 11

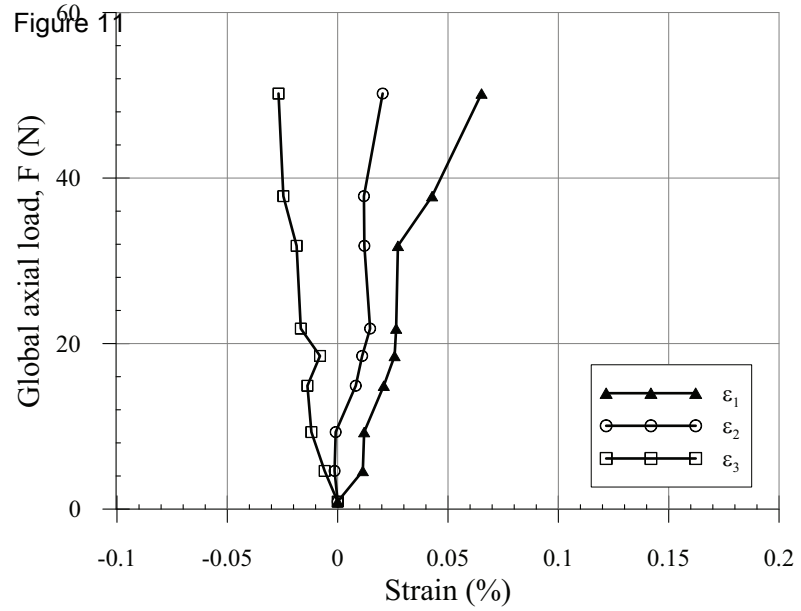

(a)

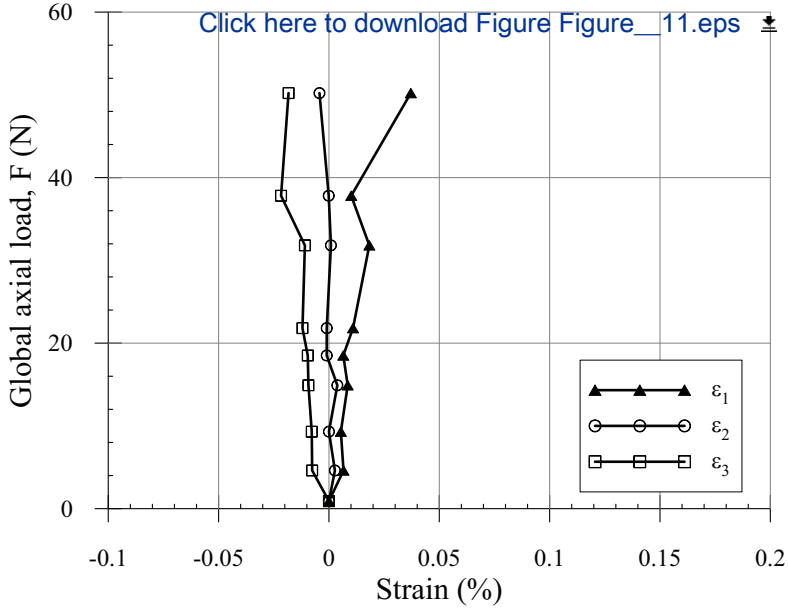

(b)

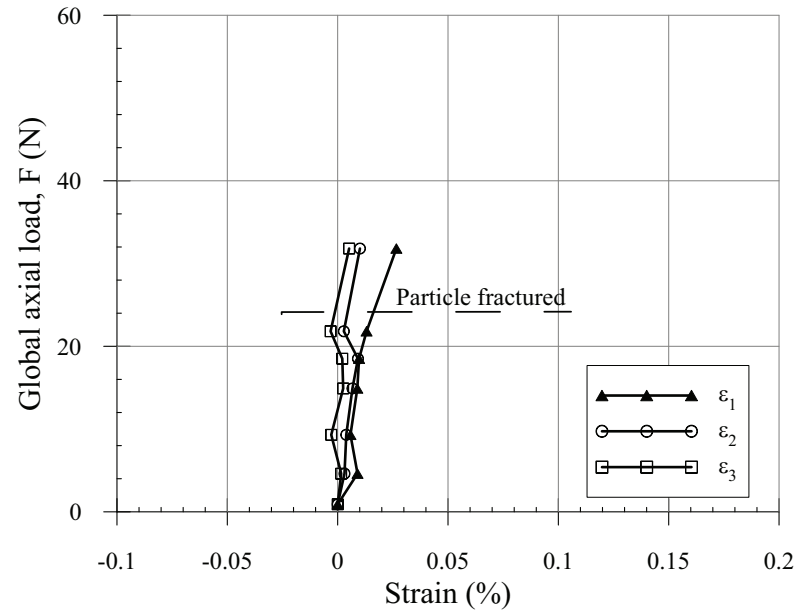

(c)

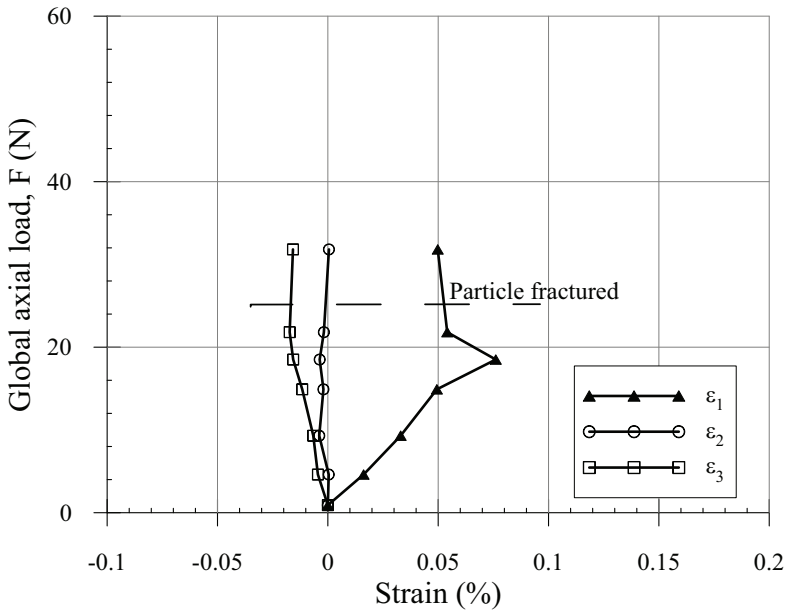

(d)

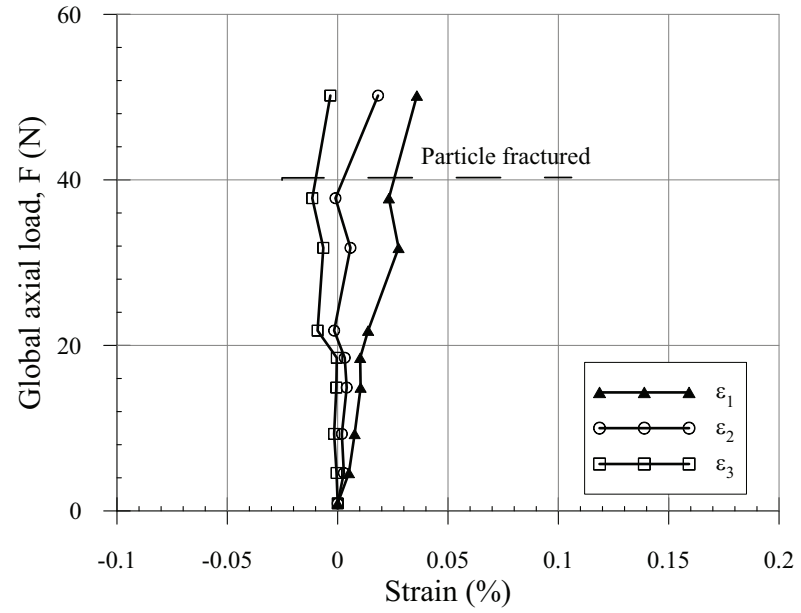

(e)

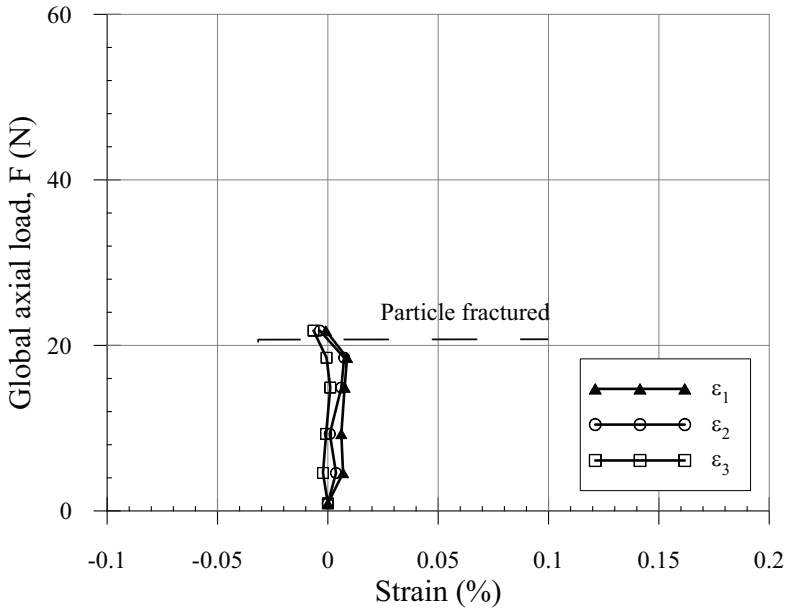

(f)

Figure 12

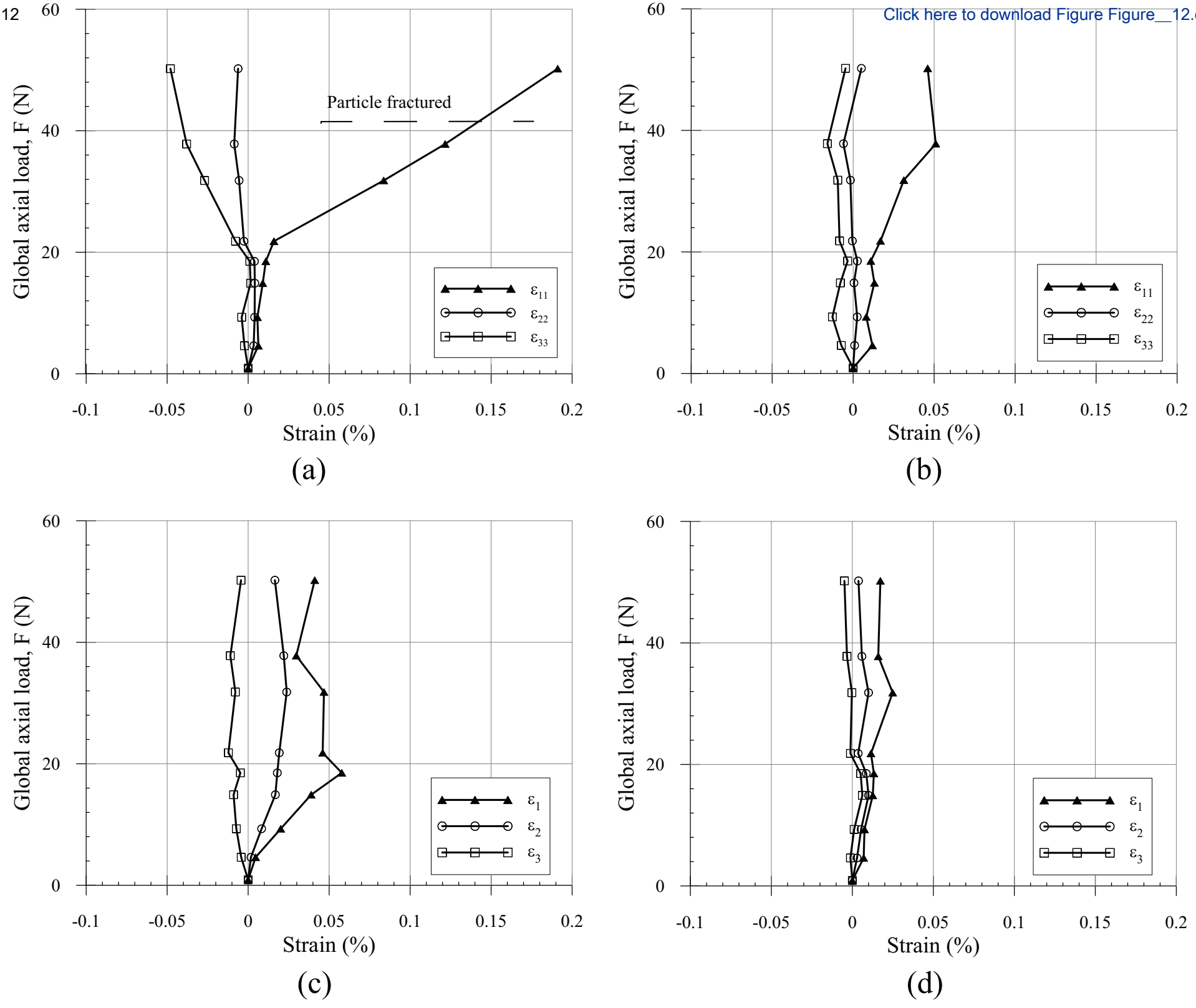

Figure 13

Click here to download Figure Figure_13.eps

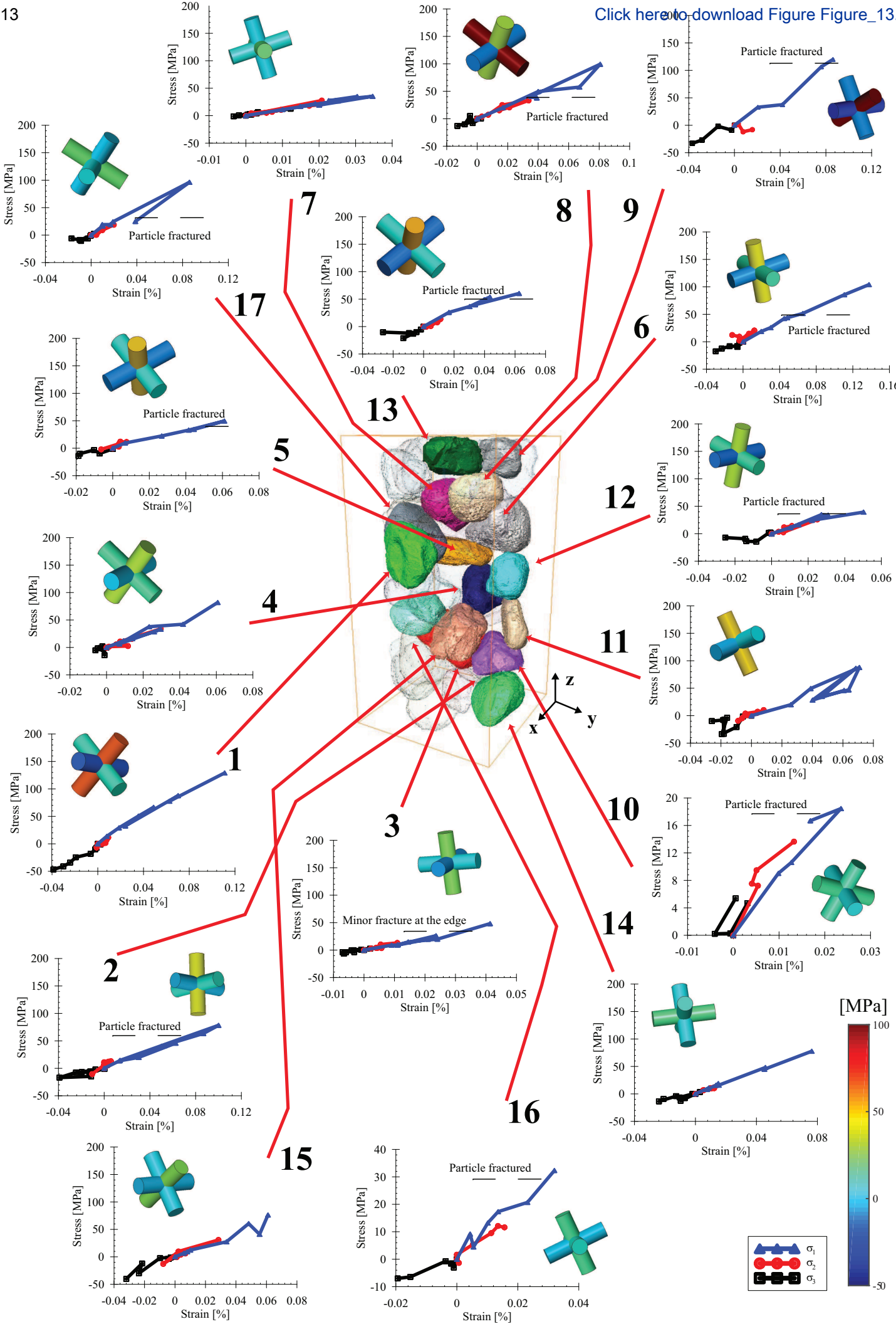

Figure 14

Click here to download Figure Figure_14.eps

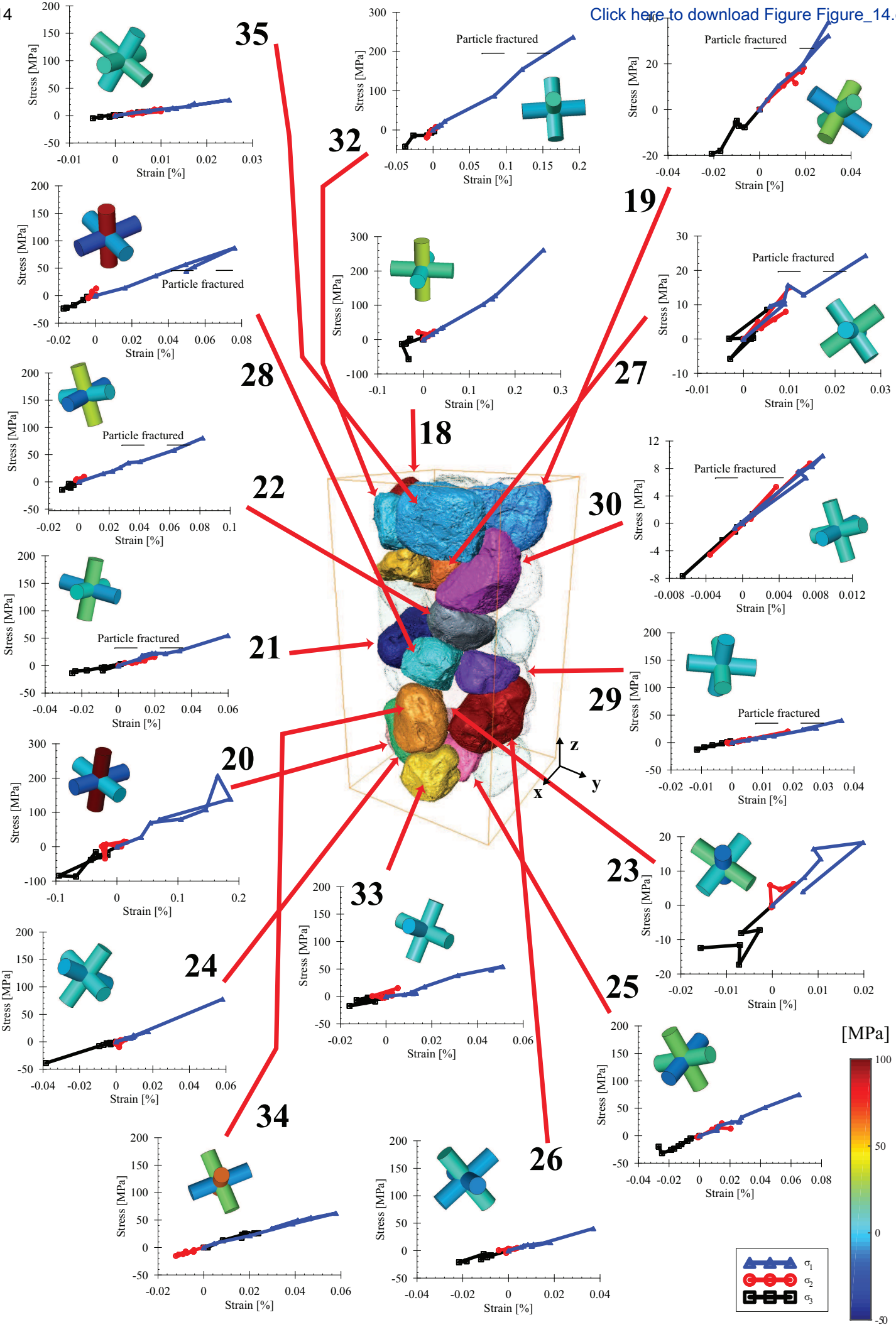

Figure 15

Click here to download Figure Figure_15.eps

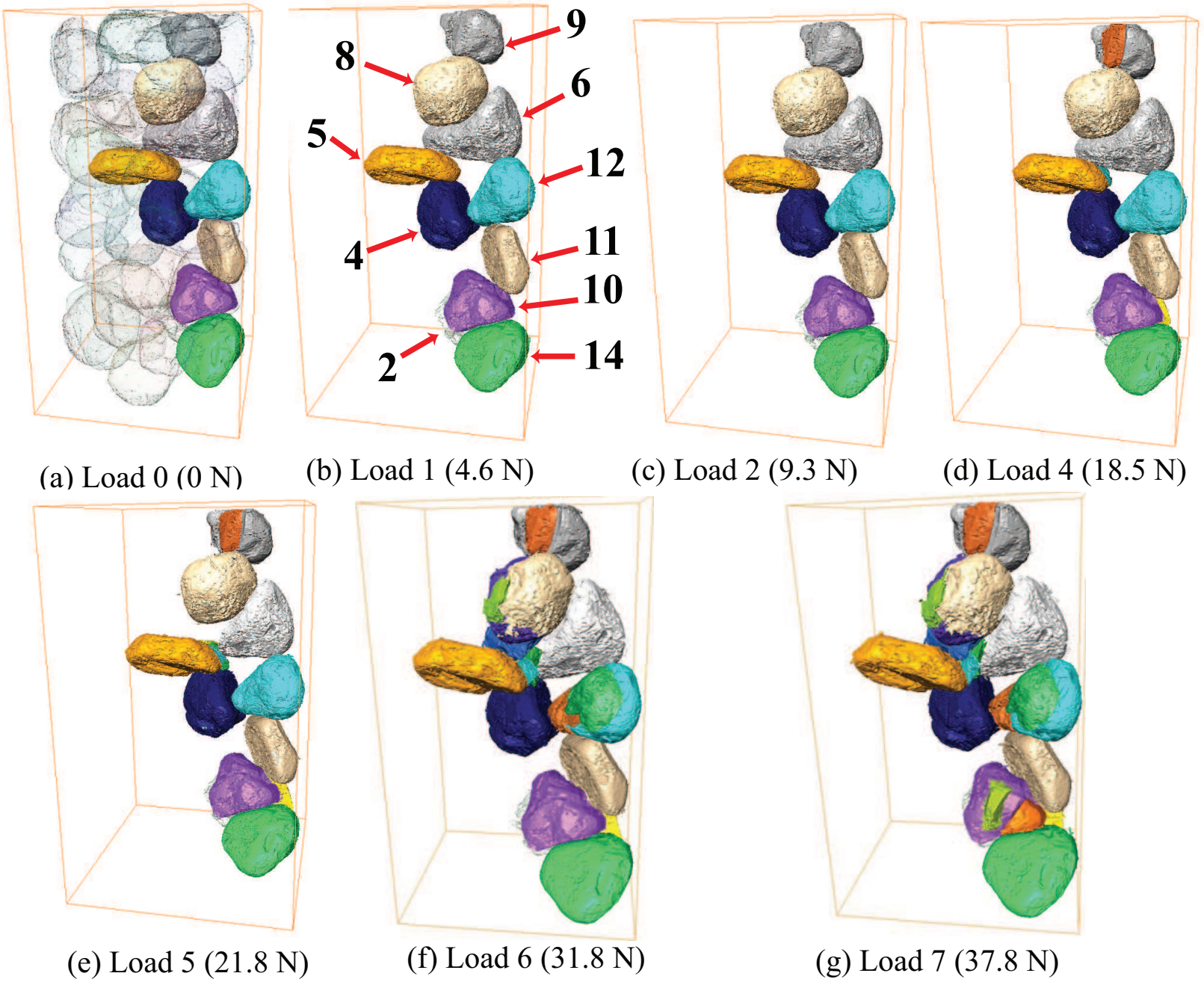

(a) Load 0 (0 N) (b) Load 1 (4.6 N) (c) Load 2 (9.3 N) (d) Load 4 (18.5 N)

(e) Load 5 (21.8 N) (f) Load 6 (31.8 N) (g) Load 7 (37.8 N)

	Coordination number (CN)					Lattice strain
Sand Particle	**Load 0**	**Load 1**	**Load 2**	**Load 4**	**Load 5**	**ε_1* (%)**
Particle 2	4	5	5	6	6	0.10
Particle 4	3	5	5	6	7	not fractured
Particle 5	6	7	7	Fractured		0.04
Particle 6	6	6	6	7	Fractured	0.05
Particle 8	7	6	6	7	8	0.08
Particle 9	5	5	5	Fractured		0.08
Particle 10	4	5	5	Fractured		0.02
Particle 11	4	4	4	5	5	not fractured
Particle 12	6	7	7	7	7	0.03
Particle 14	4	4	4	5	6	not fractured
Specimen average	5.63	6.14	6.23	6.32	6.41	

* = Highest measured ε_1 before fracture

Figure 16

Click here to download Figure Figure_16.eps

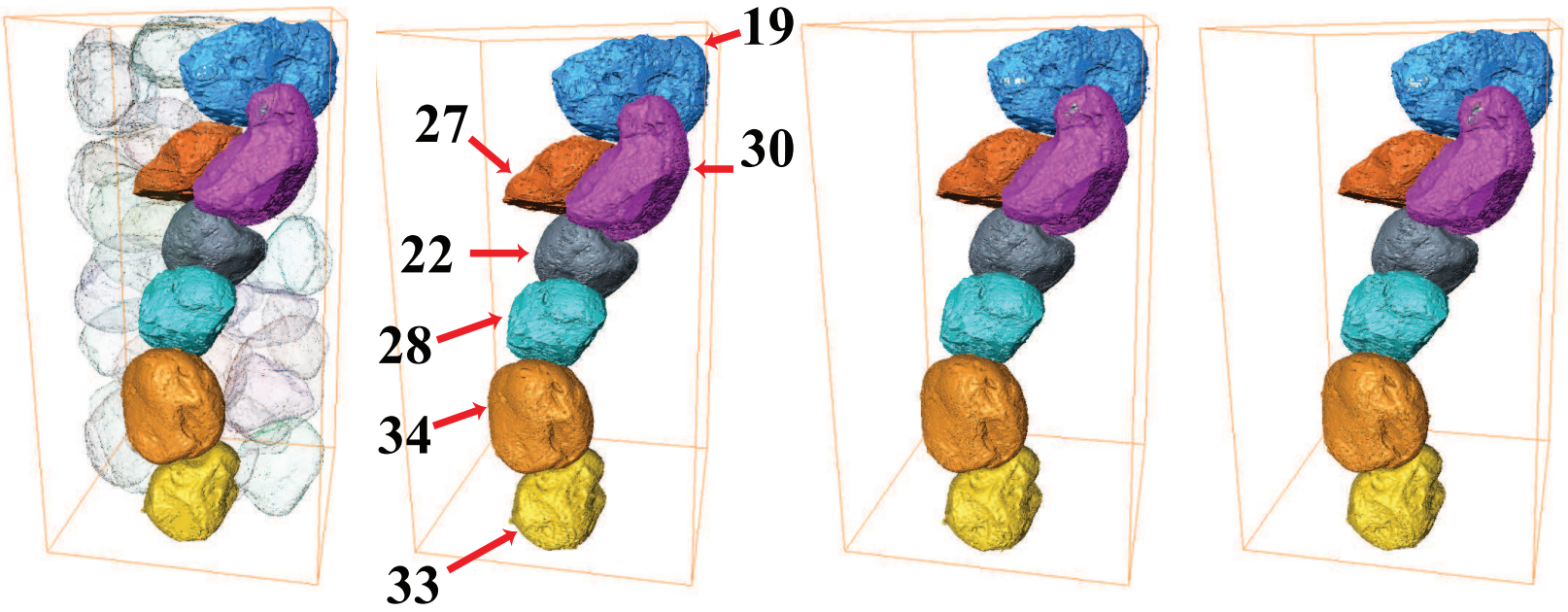

(a) Load 0 (0 N) (b) Load 1 (4.6 N) (c) Load 2 (9.3 N) (d) Load 4 (18.5 N)

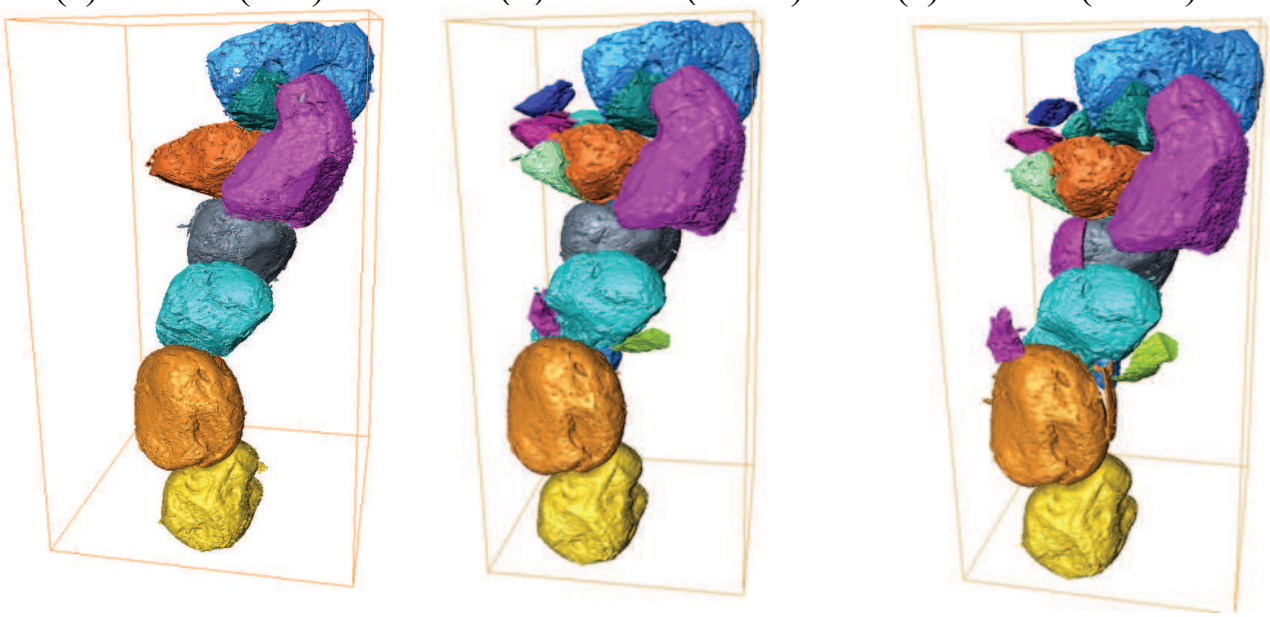

(e) Load 5 (21.8 N) (f) Load 6 (31.8 N) (g) Load 7 (37.8 N)

	Coordination number (CN)					Lattice strain
Sand Particle	**Load 0**	**Load 1**	**Load 2**	**Load 4**	**Load 5**	**ε_1* (%)**
Particle 19	8	9	9	9	Fractured	0.03
Particle 22	8	8	8	8	7	0.06
Particle 27	6	6	6	6	7	0.01
Particle 28	7	7	7	7	7	0.08
Particle 30	6	6	6	6	Fractured	0.01
Particle 33	5	5	5	6	6	not fractured
Particle 34	6	7	7	7	7	not fractured
Specimen average	5.63	6.14	6.23	6.32	6.41	

* = Highest measured ε_1 before fracture

Figure 17

Click here to download Figure Figure_17.eps

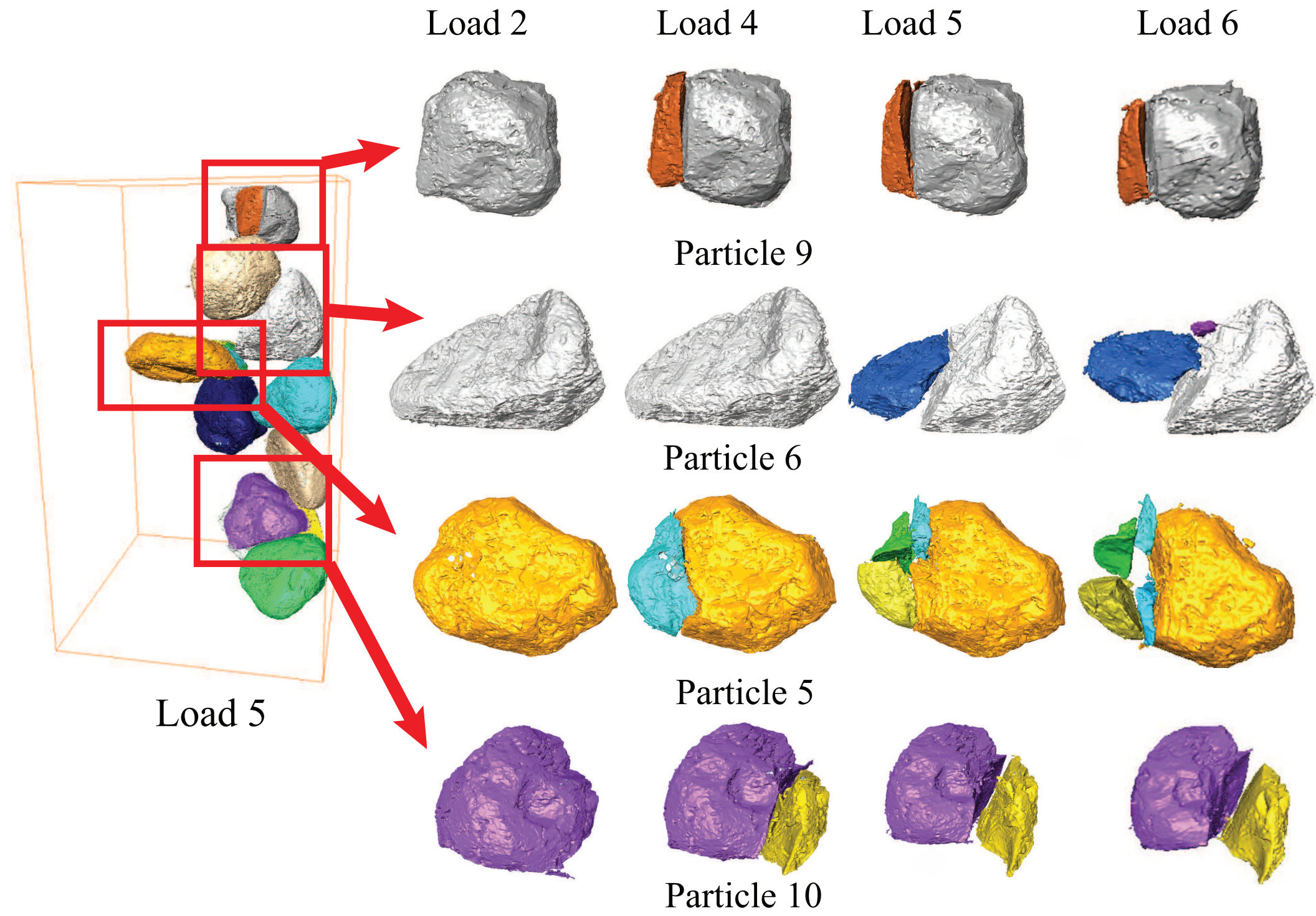

Figure 18